processes

MDPI

Article

Three-Dimensional Numerical Simulation of High-Speed Shear Crushing of High-Density Fluid

Xi Lin [1,2,*,†], Tao Lin [3,†], Gaojie Xu [1], Gangqiang Chen [2] and Fei Xu [4,*]

[1] Ningbo Institute of Materials Technology and Engineering, CAS, Ningbo 315201, China; xugj@nimte.ac.cn
[2] Ningbo Guangxin Nanomaterials Ltd., Ningbo 315099, China; gbnano@guangbo.net
[3] College of Energy Environment and Safety Engineering, China Jiliang University, Hangzhou 310018, China; m17777403617@163.com
[4] College of Metrology Measurement and Instrument, China Jiliang University, Hangzhou 310018, China
* Correspondence: lx@nanoguangbo.com (X.L.); xufei@cjlu.edu.cn (F.X.)
† These authors contributed equally to this work.

Abstract: Plasma atomization is a technology that can produce high sphericity, small particle diameters, and high-purity copper powder, which is of great significance for the development of metal additive manufacturing. At present, although plasma atomization can realize the industrial preparation of spherical copper powder, there are still some problems, such as unclear understanding of the atomization process and a lack of theoretical support for powder quality control. This leads to the inability to predict the average particle diameter of powder in advance based on the actual atomization conditions and to optimize the process parameters, which seriously affects the further development of the plasma atomization process. We mainly studied the non-stationary simulation of a DC argon plasma torch. The purpose of this paper was to study the specific influence law of the average particle diameter of the powder in the process of plasma atomization by means of numerical simulation and experimental observation. The aim was to establish the mapping relationship between the atomization condition and the average particle diameter of the powder and realize the controllable preparation of the plasma atomized powder. At the same time, we used industrial-grade plasma atomization equipment to carry out pulverizing experiments to verify the plasma atomization theory and the powder average particle diameter control scheme proposed in this paper, thus proving the reliability of this study.

Keywords: plasma atomization; powder quality control; numerical simulation

check for updates

Citation: Lin, X.; Lin, T.; Xu, G.; Chen, G.; Xu, F. Three-Dimensional Numerical Simulation of High-Speed Shear Crushing of High-Density Fluid. *Processes* **2024**, *12*, 2246. https://doi.org/10.3390/pr12102246

Academic Editor: Blaž Likozar

Received: 19 September 2024
Revised: 4 October 2024
Accepted: 10 October 2024
Published: 15 October 2024

Copyright: © 2024 by the authors. Licensee MDPI, Basel, Switzerland. This article is an open access article distributed under the terms and conditions of the Creative Commons Attribution (CC BY) license (https://creativecommons.org/licenses/by/4.0/).

1. Introduction

The production of high-quality metal powders is of great significance to meet the growing demand for metal additive manufacturing. The gas atomization method has the advantages of good sphericity, high yield of fine powder, and large production capacity [1]. Therefore, it is still the main method for preparing metal powder for 3D-printing technology [2]. Micron copper powder is a material with a scale of microns (1~100 μm). Due to its small diameter, it exhibits unique and more excellent characteristics, especially excellent electrical conductivity, thermal conductivity, specific surface area, etc., and its performance is significantly improved. At the same time, it also has a small size effect, interface effect, etc. [3,4], and it is widely used in electronics, optoelectronics, plasmonics, catalysis, catalytic cracking, thermoelectric effects and thermocouples, sensing, and biomedical fields [5–9].

The research on plasma atomization pulverizing is mainly divided into experimental research and numerical simulation research. Because the atomization process is very fast and the physical process is very complex, although some macroscopic parameters can be obtained through experiments, it is difficult to measure the details of the internal atomization flow field. Numerical simulation research can obtain detailed flow field information and become an important means of studying plasma atomization pulverizing.

Although the existing spherical powder preparation process has its own advantages, it is difficult to meet the needs of high powder purity, high fine powder yield, low irregular ball powder proportion, and low preparation cost at the same time, which limits the rapid development of metal additive manufacturing to a certain extent. In view of this, an emerging process is urgently needed to meet the production needs of low-cost preparation of high-performance spherical copper powder. In this context, plasma atomization [10] has gradually become a research hotspot in the field of powder preparation. The principle of atomization is to use high-speed airflow to crush the liquid metal flow into small droplets and quickly condense into a metal powder [11]. The powder prepared by gas atomization has a small particle size, high sphericity, low oxygen content, and good fluidity, which can be used for large-scale industrial production [12]. However, due to the novelty of the plasma atomization process itself and the complexity of the heat and mass transfer behavior in the atomization process, the current understanding of plasma atomization is not deep enough, and there is a lack of in-depth exploration of the mechanism of plasma atomization, as well as a lack of effective control methods for powder quality. This leads to some problems in the plasma atomization process, such as the difficulty in predicting the particle size or particle size distribution width of the powder [13], which seriously restricts the further development of the plasma atomization process. In 1996, Entezarian [14] first confirmed the advantages of plasma atomization in the preparation of high-quality spherical powders, and in 1997, a new atomization process (plasma atomization) was proposed for the production of fine spherical powders [15]. The process has the unique ability to produce a typical active metal spherical powder with an average particle size of 40 μm. The research and development of plasma atomization equipment systems in foreign countries started earlier. Based on the scheme of Entezarian [15], the Pyrogenesis Company in Canada [16] proposed a relatively mature plasma atomization equipment system and published a patent in 2018. In this patent, the Pyrogenesis Company used induction power supply to preheat the wire, optimized the powder collection device, and realized the industrial powder production in the true sense of plasma atomization. Subsequently, a patent [17] was applied in 2019, and a new crushing technology combining plasma atomization and arc-spraying technology was proposed, which took into account both the powder performance and powder extraction rate. In comparison, the research on plasma atomization pulverizing by domestic companies is still in its infancy, which also reflects the urgent need to optimize the process parameters of plasma atomization pulverizing from the heat and mass transfer behavior of plasma atomization itself.

The quality of the atomized powder depends largely on the plasma torch that produces the plasma jet. Yin et al. [18] carried out experimental and numerical studies on the self-made reverse polarity plasma torch (RPT). The results showed that the RPT worked stably in the arc voltage mode within 10 V, which ensured the uniform quality of the prepared powder. It also showed the effectiveness of the RPT in the production of high-quality powder with a smooth surface, high sphericity, and small particle size. Dorval et al. [16] disclosed a device and process for producing high-purity powder at high capacity from wire using a combination of plasma torches and induction heating. Based on the process experiment results, it was found that the diameter of the wire and the angle between the jet and the wire greatly affected the atomization efficiency. After further analysis of the experimental results, it was found that increasing the current flow of the plasma generator could also significantly increase the powder yield, but it would lead to an increase in the average particle diameter of the powder. Wang et al. [19] prepared FGH98 alloy powder using the plasma rotating electrode method. Starting from the optimization of process parameters, the effects of the main preparation process parameters, such as the bar diameter and bar rotation speed, on the average particle size and distribution of the powder were studied, and the optimum powdering process conditions were explored.

Based on the above background, this paper aims at the preparation of a copper powder using the plasma torch atomization method proposed by Ningbo Guangxin Nanomaterials Ltd. The particle diameter distribution, powder morphology, and properties of the

powder are studied to try and obtain the best production process parameters. This paper is organized as follows: In Sections 2 and 3, a three-dimensional plasma torch–liquid guide tube numerical model is established, and in Section 4, the industrial-grade plasma atomization equipment pulverizing experimental results are compared with the plasma torch atomization simulation to verify the reliability of the simulation. In Section 5, we adjust the variables one-by-one to study the influence of the plasma velocity, V_1, the shape of the liquid duct outlet, the surface tension, σ, the length of the collection tube, L, the chamfering, and the vertical distance, L_1, from the end of the liquid guide tube to the center of the plasma torch outlet on the shear atomization and the particle size distribution of the powder. In this paper, the in-depth study of plasma atomization reveals the relationship between the process parameters and the quality of the spherical copper powder, realizes the accurate control of the quality of the spherical copper powder, improves the output of the high-quality spherical copper powder, and further promotes the development of metal additive manufacturing, as well as realizes the double improvement of economic benefits and production technology.

2. Numerical Model

The atomization process is a complex process. When the fluid is unstable under the action of high-speed airflow, a tear in the liquid film and breakup of the droplets are produced. In the external environment, the broken droplets overcome the effect of their own internal forces (surface tension and viscous force) to further break, and finally achieve atomization.

The Lagrangian particle-tracking method and interface capture method are two typical methods for the numerical solution of the atomization process. The Lagrangian particle-tracking method is mainly realized by the discrete phase model (DPM). In the DPM, the liquid phase is regarded as a discrete particle, and the atomization process is simulated by tracking the velocity, position, momentum, and other information of the particles, combined with the sub-models, such as the droplet breakup model and the aggregation model [20,21]. This method is relatively mature and has a small amount of calculation, so it has been widely used in the simulation of the jet atomization process [22,23]. Although the calculation amount of the DPM for solving the jet atomization process is small, the interaction between the gas and liquid phases is only reflected in the source term of the Euler equation, so the whole process of atomization cannot be truly restored; especially, the specific information of the primary atomization process is ignored. The interface capture method obtains the position information of the gas–liquid two-phase interface by analyzing the phase interface, so as to realize the direct solution of the jet atomization process. The commonly used interface capture methods include the volume of fluid (VOF) method [24,25] and the level set method (LS) [26,27]. Although the interface capture method can provide detailed information about the atomization process, it has high requirements on the quality of the grid and requires a sufficiently fine grid to capture the droplets generated during the atomization process, which often leads to a huge amount of calculation.

In order to solve this problem, researchers have proposed a new method combining the advantages of the VOF and DPM. The VOF-DPM [28–30] uses the VOF to solve continuous liquid columns and large droplets, while for smaller droplets, they are solved by DPM. In this way, the method can not only capture the movement and deformation of the phase interface in the initial stage of atomization, but also convert small droplets of a certain size into Lagrangian particles according to a certain conversion mechanism, thus effectively reducing the amount of calculation.

Based on the above assumptions, the governing equations involved in the simulation of plasma moment high-speed shear atomization in this paper are outlined below [31].

Mass conservation equation:

$$\frac{\partial \rho}{\partial \mathrm{t}} + \nabla \cdot (\rho \vec{v}) = 0 \tag{1}$$

Momentum conservation equation:

$$\frac{\partial\left(\rho\vec{v}\right)}{\partial t}+\nabla\cdot\left(\rho\vec{v}\vec{v}\right)=-\nabla P+\nabla\cdot\tau+\rho g+F_{\sigma} \tag{2}$$

Energy equation:

$$\frac{\partial(\rho e)}{\partial t}+\nabla\cdot\left(\rho\vec{v}e\right)=-\nabla\cdot\left(P\vec{v}\right)+\nabla\cdot\left(\tau\vec{v}\right)-\nabla\cdot q \tag{3}$$

Continuity equation:

$$\frac{\partial(\rho_i\alpha_i)}{\partial t}+\nabla\cdot\left(\rho_i\vec{v}_i\alpha_i\right)=0 \tag{4}$$

where, ρ is the density (kg/m^3), t is the time (s), $\vec{v}$ is the velocity vector (m/s), P is the scalar pressure (Pa), τ is the viscous stress tensor, $\vec{g}$ is the gravitational acceleration (m/s^2), F_{σ} is the volume surface tension (N/m), e is the total energy (J), t is the temperature (K), c_v is the specific heat capacity (J/(kg·K)), and q is the heat flux density of heat conduction (J/(s·m^2)). In the VOF model, the ρ and $\vec{V_1}$ values in Equations (2)–(4) are weighted by the volume fraction of each phase. α_i, ρ_i, and $\vec{v_i}$ are the volume fraction, density, and velocity of the i phase, respectively.

The multiphase flow model is a coupling model of the VOF to DPM provided by Fluent, which realizes the continuous simulation of the atomization process. The coupling model of the VOF to DPM combines the advantages of the VOF method and the Euler–Lagrangian method. Firstly, the VOF method [32,33] is used to simulate the initial jet flow and jet breakup. In the atomization region, the DPM [34,35] is used to track the flight trajectory of the droplets. The model conversion of the coupling model in the calculation process is based on whether the liquid block meets the conversion criteria, such as the liquid block size, asphericity, and liquid volume fraction, set by the user in the atomization calculation. If satisfied, the liquid block will be removed from the VOF model and appear in the form of particle packets in the DPM, and the DPM continues to track the trajectory of the particle packets.

$$\frac{\partial}{\partial t}\left(\rho\vec{v}\right)+\nabla\cdot\left(\rho\vec{v}\vec{v}\right)=-\nabla P+\left[\mu\left(\nabla\vec{v}+\nabla\vec{v}^{T}\right)\right]+\rho\vec{g}+\vec{F}(1) \tag{5}$$

The VOF-DPM coupling model is used to simulate the high-speed shear atomization process of copper ions. The volume of fluid (VOF) method, proposed by Hirt et al. [36], is used to track the gas–liquid interface of copper ions in the atomization flow field. The momentum equation of each phase in the whole region is solved, and the weighted average is carried out. The single momentum equation shared by each phase is obtained, and the obtained velocity field is shared by each phase.

Here, $\vec{v}$ is the velocity of the liquid phase, P is the pressure, ρ and μ are the density and dynamic viscosity, respectively, and F is a source term, which can be replaced by surface tension.

The DPM can simulate various problems involving discrete phases. During the atomization process of copper ion particles, the volume fraction must be less than 10%, which is also in line with the application of the DPM. The force balance equation of the particles in the Cartesian coordinate system (x direction) is as follows:

$$\frac{du_p}{dt}=F_{\mathrm{D}}(u-u_p)+\frac{g_x(\rho_{\mathrm{p}}-\rho)}{\rho_p}+F_x \tag{6}$$

where F_D $(u - u_p)$ is the drag force per unit mass of particles.

$$F_D = \frac{18\mu}{\rho_p {d_p}^2} \frac{C_D \mathrm{Re}}{24} \tag{7}$$

Here, u is the fluid phase velocity, u_p is the particle velocity, μ is the fluid dynamic viscosity, ρ is the fluid density, ρ_p is the particle density (skeleton density), d_p is the particle diameter, and Re is the relative Reynolds number (particle Reynolds number).

3. Geometric Model

3.1. Physical Model

In this paper, the atomization process of droplets in the area near the liquid guide tube was studied. The high-temperature and high-speed fluid produced by the high-temperature plasma torch was used to shear the liquid Cu. After the liquid Cu was sheared by the high-temperature and high-speed fluid generated by the plasma torch, an irregular liquid column was first formed, and then the liquid column was further sheared and broken by the high-speed fluid generated by the plasma torch at the edge to form an irregular liquid block. When the liquid block met the conversion criteria set by the liquid block size, asphericity, liquid volume fraction, etc., the liquid block was removed from the VOF model and appeared in the form of particle phase in the DPM; that is, the irregular liquid block further condensed under the interfacial tension to form broken droplet particles. The diameter of the formed particles was proportional to the liquid blocks with different diameters. The smaller the volume of the liquid block, the smaller the diameter of the formed droplet particles.

According to the previous physical application, the liquid guide tube–plasma torch was selected as the geometric model of this numerical simulation. In order to speed up the calculation efficiency and stability, simplify the original model, and retain the geometric structure of the liquid guide tube and the plasma distance outlet, this paper established a numerical model of three-dimensional plasma distance high-speed shear atomization through Space Claim. The liquid Cu flowed out from the outlet of the liquid guide tube, and then sheared and collided with the plasma jet that flowed out at a high speed in the horizontal direction, so that the liquid block was broken into a particle phase and discharged through the outlet of the liquid guide tube. As shown in Figure 1, the model consisted of two parts: the liquid guide tube and the plasma torch. The liquid guide tube presented a flared shape, while the plasma torch presented a cylindrical shape. The inner diameter of the liquid guide tube outlet was 1 mm, and the plasma distance was 4 mm. In order to save computing resources, the calculation area L × H = 120 mm × 60 mm. The computational grids were unstructured grids, and the initial number of grids was 106,039. The minimum mesh size of the outlet area of the liquid guide tube was 0.02 mm, and the minimum mesh size of the outlet area of the plasma torch was 0.2 mm, as shown in Figures 2 and 3. The adaptive grid was set to 10 μm.

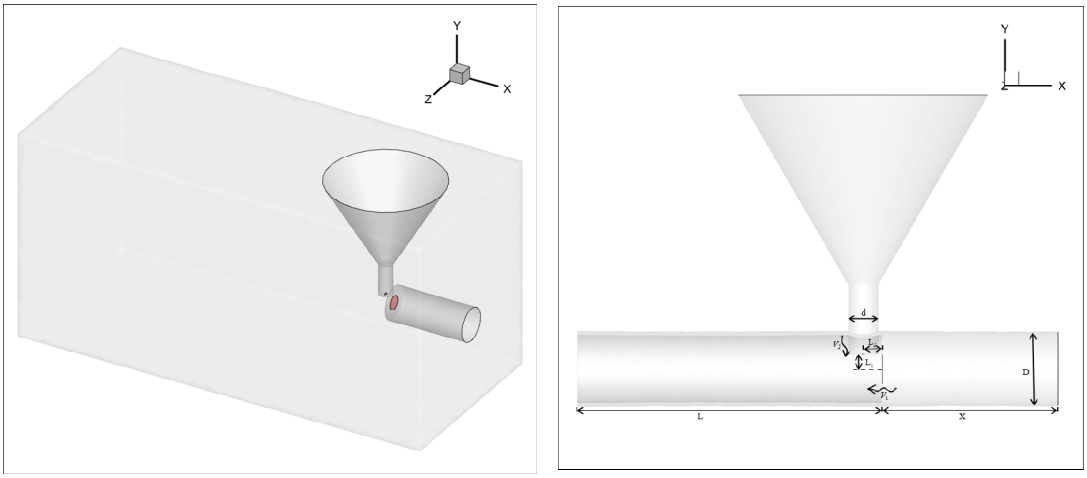

Figure 1. Overall structure diagram (including the computational domain) (**left**) and variable parameters involved in the model (**right**).

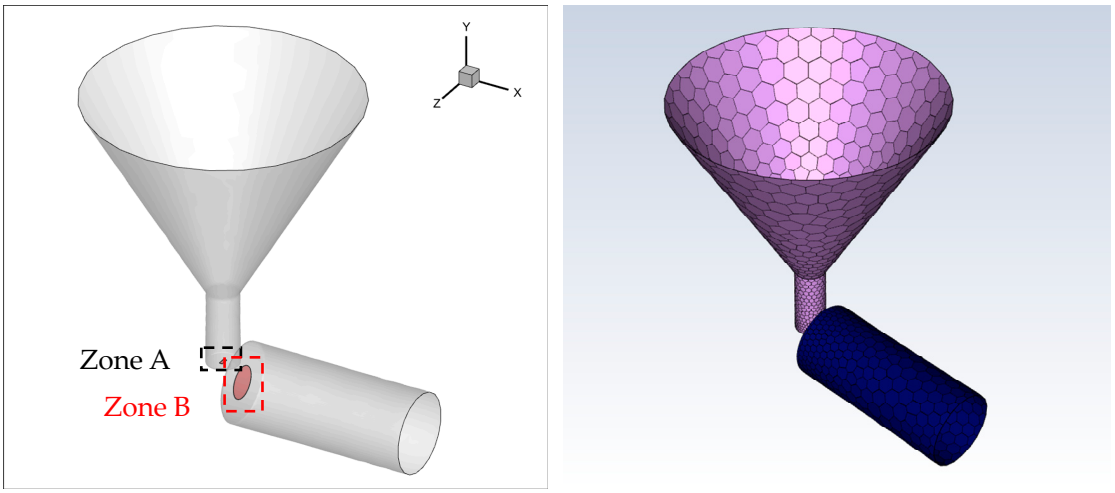

Figure 2. Liquid tube–plasma torch model (**left**) and liquid tube–plasma torch model grid diagram (**right**).

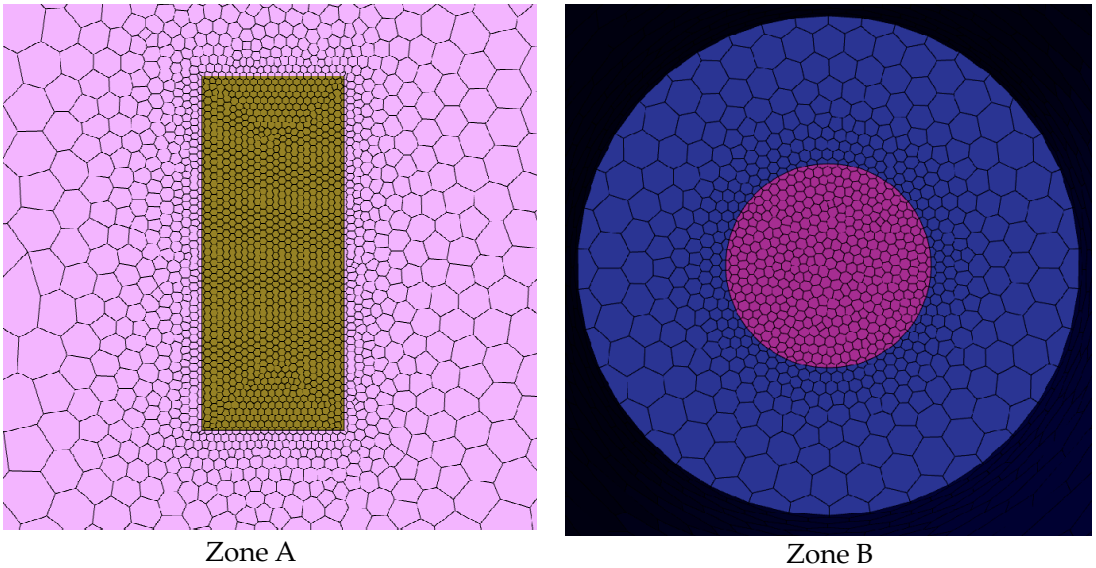

Figure 3. Liquid tube outlet (Zone A) and plasma torch outlet (Zone B) local encryption grid detail diagram.

3.2. Boundary Conditions and Parameter Settings

The SIMPLE algorithm was used to solve the problem of pressure–velocity coupling, and the pressure-based solver was selected to simulate the flow at the outlet of the liquid guide tube and its vicinity. Argon (Ar) was set as the first phase and liquid Cu as the second phase on the VOF model. The discrete phase model was used, and the continuous surface force model was applied as the surface tension model. The surface tension coefficient between Ar and liquid Cu was set to 0.074 N/m. The calculation area adopted the pressure outlet boundary condition, the pressure value was set to the standard atmospheric pressure of 0.1 MPa, and the inner wall of the liquid pipe was applied with no slip characteristics. The velocity mixing inlet boundary condition was selected at the inlet of the pipe, and the velocity was 1 m/s. Due to the viscous dissipation theory of turbulence, the turbulence model was set as the k-omega model. The plasma inlet also selected the velocity mixing inlet boundary condition, and the velocity was 498.25 m/s. The value was calculated by using the specific experimental condition parameters (Table 1).

Table 1. Specific experimental condition parameters.

Anode Length	Anode Inner Diameter	The Rotation Angle of Gas Distributor	Dielectric Gas	Intake Pressure	Wall Temperature	Anode Potential	Cathode Potential
23 mm	4 mm	30°	100% Ar	0.879 MPa	300 K	400 V	−400 V

By adjusting the variables one-by-one, the effects of the plasma distance from the outlet speed, the outlet shape of the liquid guide tube, the surface tension, the length of the collection tube, the chamfering, and the vertical distance, L_1, from the end of the liquid guide tube to the center of the plasma torch outlet on the shear atomization effect were studied. The variable parameters involved in the specific CFD simulation are shown in Table 2.

Table 2. The main parameters of the CFD simulation.

	L_1 (mm)	L_2 (mm)	d (mm)	D (mm)	V_1 (m/s)	V_2 (m/s)	σ (N/m)	Outlet Shape of Liquid Pipe	L (mm)	Chamfer
Case 1	2	2.5	1	4	498.25	1	0.074	1 × 0.2 rectangle	0	×
Case 2	2	2.5	1	4	498.25	1	0.074	1 × 0.4 rectangle	0	×
Case 3	2	2.5	0.72	4	498.25	1	0.074	d = 0.72 mm circle	0	×
Case 4	2	2.5	1	4	1000	1	0.074	1 × 0.4 rectangle	0	×
Case 5	2	2.5	1	4	1500	1	0.074	1 × 0.4 rectangle	0	×
Case 6	2	2.5	1	4	498.25	1	0.74	1 × 0.4 rectangle	0	×
Case 7	2	2.5	1	4	498.25	1	0.074	1 × 0.4 rectangle	40	×
Case 8	2	2.5	1	4	498.25	1	0.074	1 × 0.4 rectangle	0	√
Case 9	0	2.5	1	4	498.25	1	0.074	1 × 0.4 rectangle	0	×
Case 10	1	2.5	1	4	498.25	1	0.074	1 × 0.4 rectangle	0	×

Table 3 shows the model selected for the numerical calculation of the spray atomization process based on the VOF-DPM method coupled with the flow at the outlet of the liquid duct. In this study, for the setting of VOF-DPM, the minimum volume equivalent diameter was set to 0 mm, and the maximum volume equivalent diameter was set to 0.6 mm. The standard deviation of the normalized radius and the surface orthogonality of the average radius were selected at the default value of 0.45.

Table 3. Shear atomization model.

Equation solver	Transient, First-Order Implicit
Multiphase flow model	VOF-DPM
Turbulent flow model	SST k-Omega, Stress-Blended Eddy Simulation (SBES) Model

4. Experimental Verification

In the performance test experiment of the plasma torch generator, in order to study the influence of the outlet shape of the liquid guide tube on the particle size formed by the shear atomization of liquid Cu, the experimental parameters, such as those in Tables 4 and 5, were designed, where d is the inner diameter of the circular outlet of the liquid guide tube.

Table 4. Design parameters.

Experimental Name	L (mm)	L_1 (mm)	L_2 (mm)	d (mm)	D (mm)	X (mm)
Sample	0	2	2.5	1	5	23

Table 5. Plasma torch operating parameters.

Experimental Name	Gas Component	Gas Flow (m^3/h)	I (A)	U (V)	P (kW)	The Proportion of Powder over a 400-Mesh Sieve (%)
Sample	Ar	14.4	149	63	9.4	39.5

The whole plasma torch atomization pulverizing experiment was carried out at Ningbo Guangxin Nanomaterials Ltd., and the team was led by Dr. Lin Xi to complete it. Our experiment used a conventional industrial-grade plasma atomization equipment system, without the constraint structure of the collection tube. The inner diameter of the liquid guide tube was 1 mm, the inner diameter of the plasma torch was 5 mm, and the anode length of the plasma torch was 23 mm. The vertical distance from the end of the liquid guide tube to the center of the plasma torch outlet was set to 2 mm, and the horizontal distance from the center of the liquid guide tube to the end of the plasma torch outlet was set to 2.5 mm. Before the atomization experiment, it was necessary to vacuumize and replenish the gas to ensure the purity of the powder to the maximum extent. In the experiment, Ar was introduced, the gas flow rate was 14.4 m^3/h, the current was 149 A, the voltage was 63 V, and the power was 9.4 kW. After the calculation and analysis of the parameters of the experimental conditions, the outlet velocity of the plasma torch in the simulation was 498.25 m/s. In the process of pulverizing, the valve of the collection pipe was in the open state to discharge the excess argon gas, so as to ensure that the internal pressure of the furnace body was always maintained at an atmospheric pressure. When the milling was completed, the fan was started, and the powder was taken, with argon, to the powder tank. At this time, the heavier powder was collected, and the lighter impurities were blocked by the filter. At the same time, the fan outlet discharged pollution-free argon. The powder samples obtained in this experiment accounted for 39.5% of the proportion of

powder over a 400-mesh sieve. The specific design parameters and plasma torch operating parameters are shown in Tables 4 and 5.

$$r = \frac{\sum_{i=1}^{n}(x_i - x_{ave})(y_i - y_{ave})}{\sqrt{\sum_{i=1}^{n}(x_i - x_{ave})^2}\sqrt{\sum_{i=1}^{n}(y_i - y_{ave})^2}} \quad (8)$$

During the experiment, the gas supply system and cooling system were connected first, and then the plasma power supply was turned on to generate a plasma torch. After setting the voltage and current values of the power supply, the power supply was turned on, an arc was generated between the two wires, and the Cu powder was prepared by atomization. Firstly, to better verify the simulation, the dimensionless particle diameter x (x = particle diameter/maximum particle diameter) was defined. In order to verify the reliability of our proposed simulation as much as possible, a set of simulation conditions that were basically consistent with the experimental conditions (the shape of the outlet of the liquid guide tube was a circle, with d = 0.72 mm) was selected to compare the particle diameter distribution. In the system of high-speed shear atomization of liquid Cu by plasma torch gas, the outlet shape of the liquid pipe was a circle, with d = 0.72 mm. From the frequency distribution curve of the dimensionless particle diameter parameter x in Figure 4, it can be seen that in the experiment and simulation, the dimensionless particle diameter x of the particles formed by the plasma torch high-speed shear liquid Cu atomization was mainly concentrated between 0.3 μm and ~0.6 μm. The particle diameter of the powder showed an approximately normal distribution, and the distribution was more concentrated. Although the proportion of the particle diameter obtained by the experiment was slightly higher than that of the simulation (0.117), which was 0.135, it was roughly close to the simulation prediction results. According to Equation (8), the correlation coefficient between the experiment and the simulation and the dimensionless particle size was as high as 0.995 (0.926), which further proves the reliability of our model for the simulation of the plasma torch high-speed shear atomization liquid Cu.

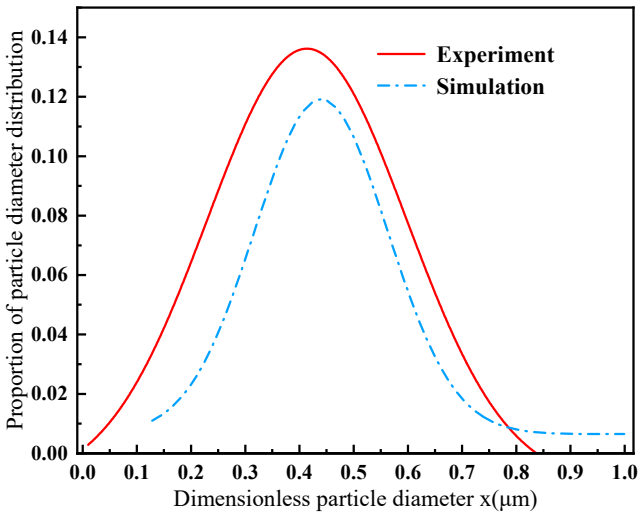

Figure 4. The particle size distribution curves of equivalent particle sizes in the experiment (red) and simulation (blue).

The morphology of the Cu powder prepared by the plasma atomization device developed by our company is shown in Figure 5. It can be seen from Figure 5 that the Cu powder prepared by the plasma atomization device designed in this paper had the following characteristics. First, the sphericity of the powder was high, and the particle diameter of the powder was basically below 36 μm. In addition, the particle diameter distribution of the Cu powder prepared in this paper was relatively concentrated, and there were individual powder particles with larger particle diameters. This may be due to the fluctuation of the

arc, which caused some droplets to leave the high-speed region of the plasma torch before they were completely broken. From the experimental results, it can be seen that the plasma atomization method used a high-temperature and high-speed plasma torch to break the Cu metal molten liquid, which ensured the superheating of the powder particles; thus, it had a sufficient spheroidization and solidification time, so the sphericity was good. The high-temperature and high-speed plasma airflow had a sufficient impact of kinetic energy to fully break the molten metal liquid and reduce the average particle diameter, and the particle diameter distribution range was small.

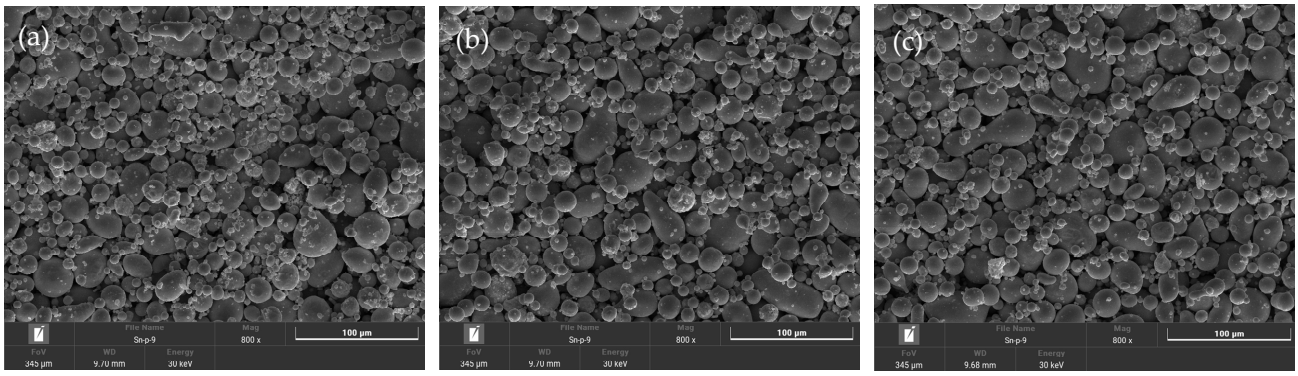

Figure 5. (**a**–**c**) The morphology of the prepared Cu powder sample.

5. Analysis and Discussion

5.1. Plasma Torch Exit Velocity, V_1

As shown in Figure 6a, after the liquid column was subjected to high-speed shear by the plasma torch, an irregular liquid column was formed first, and the liquid column was further sheared and broken by the plasma torch at the edge to form an irregular liquid block. When the liquid block met the set conversion standards, such as liquid block size, asphericity, liquid volume fraction, etc., the liquid block was deleted from the VOF model and appeared in the form of particle phase in the DPM; that is, the irregular liquid block was further condensed under the interface tension to form broken droplet particles. The diameter of the formed particles was proportional to the diameter of the liquid phase in different diameters. The smaller the volume of the liquid block, the smaller the particle diameter. As shown in Figure 6b, the particle diameter distribution range formed at three different plasma torch speeds was 8 μm~48 μm, of which the particles with a particle diameter between 8 μm and ~24 μm accounted for the vast majority (about 90%), and a small part of the particle diameter was distributed between 24 μm and ~48 μm. The larger the slope of a point on the curve, the larger the proportion of the small particle diameter. When V_1 = 1500 m/s (the ratio of the outlet velocity of the plasma torch gas to the outlet velocity of the liquid Cu in the liquid guide tube was 1500), the cumulative distribution curve of the particle diameter tended toward 1 faster (compared to V_1 = 500 m/s and V_1 = 1000 m/s), and with the increase in the plasma moment outlet velocity V_1, the proportion of particles in the particle diameter range of 8 μm~16 μm was larger. Therefore, the increase in the plasma moment outlet velocity tended toward the generation of small-diameter particles.

From the velocity contours of Figure 7a–c, it can be seen that the outlet velocity of the fluid at the bottom of the liquid pipe was below 50 m/s, while the outlet velocity of the plasma moment gas was about 500 m/s, 1000 m/s, and 1500 m/s, respectively, so the fluid velocity was much smaller than the gas velocity. There was a velocity difference between the liquid pipe fluid and the plasma moment gas, and the liquid phase fluid was sheared and broken. The greater the velocity gradient, the greater the shear effect of the liquid phase fluid, so it was broken in time to form a particle phase, and did not produce a large liquid phase block, as shown in Figures 8 and 9 for the dU/dY and dU/dZ gradient diagrams. Figure 8 shows that, from left to right, the velocity gradient became gradually

dense, and in Figure 9, the velocity gradient became gradually dense from top to bottom. From the velocity vector distribution of the flow field, it can be seen that at the XY section, the flow direction of the fluid gradually changed from longitudinal to transverse, forming a vortex, and with the increase in the plasma moment outlet velocity V_1, the greater the transverse velocity, the better the shear effect of the liquid phase fluid. Therefore, the increase in the plasma moment outlet velocity was beneficial to the shear breakage of the liquid phase fluid.

L_1 (mm)	L_2 (mm)	d (mm)	D (mm)	X (mm)	Medium	V_1 (m/s)	V_2 (m/s)	Outlet Shape of Guide Pipe	Adaptive Mesh (μm)
2	2.5	1	4	23	100% Ar	500	1	1 mm × 0.4 mm rectangle	10
2	2.5	1	4	23	100% Ar	1000	1	1 mm × 0.4 mm rectangle	10
2	2.5	1	4	23	100% Ar	1500	1	1 mm × 0.4 mm rectangle	10

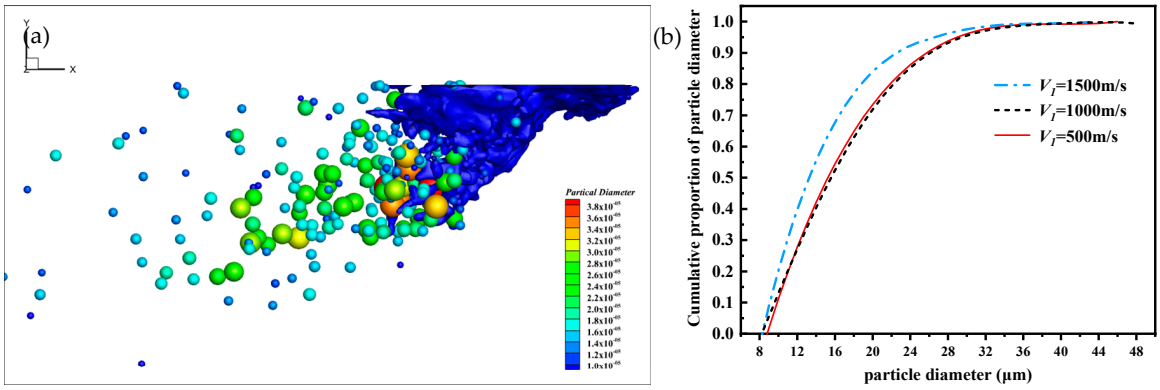

Figure 6. (**a**) Spatial distribution of liquid particles. (**b**) Particle diameter distribution curve.

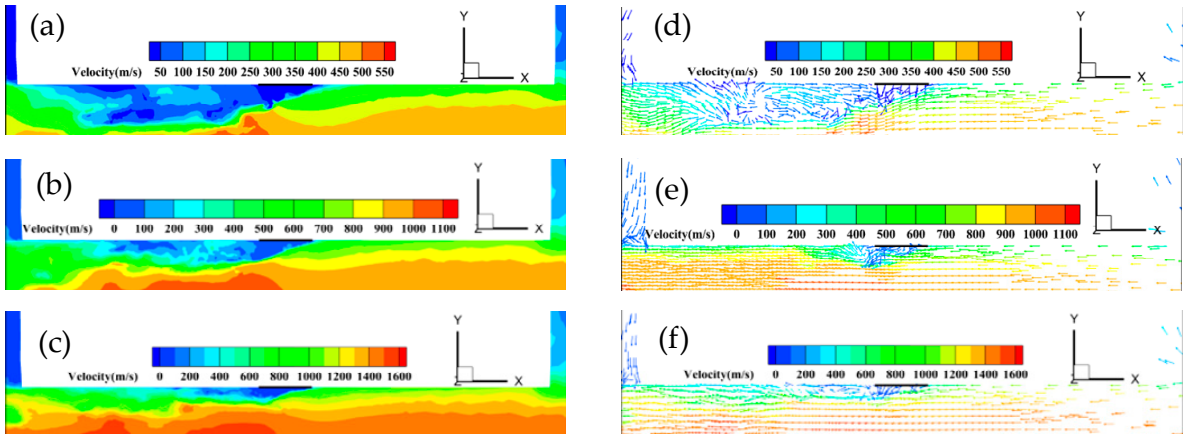

Figure 7. (**a**,**d**), (**b**,**e**), (**c**,**f**) The velocity nephogram and velocity distribution vector diagram when V_1 = 500 m/s (first row), 1000 m/s (second row), and 1500 m/s (third row), respectively.

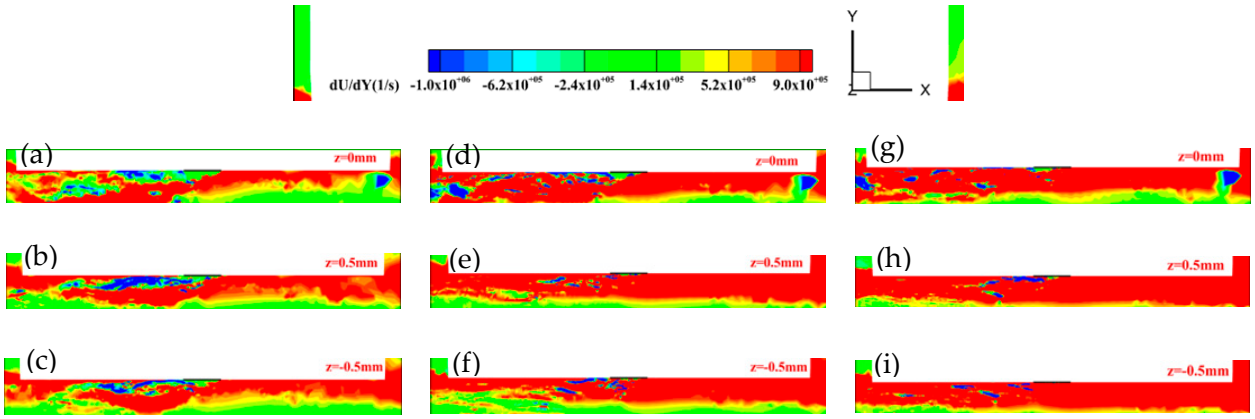

Figure 8. (**a**–**c**) For V_1 = 500 m/s (first column), X-direction velocity on the Y-axis of the gradient cloud, and similarly for (**d**–**f**) V_1 = 1000 m/s (second column) and (**g**–**i**) V_1 = 1500 m/s (third column).

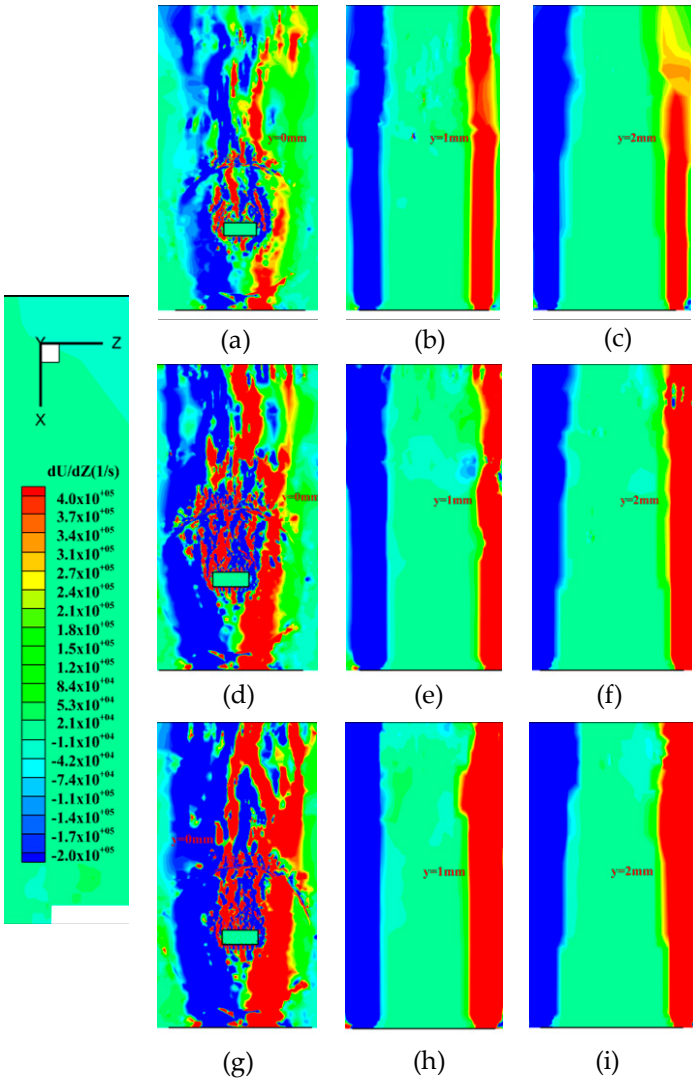

Figure 9. (**a**–**c**) The gradient cloud diagram of the velocity in the X-direction on the Y-axis when V_1 = 500 m/s (first row); similarly, (**d**–**f**) V_1 = 1000 m/s (second row) and (**g**–**i**) V_1 = 1500 m/s (third row).

5.2. Outlet Shape of Liquid Pipe

As shown in Figure 10a, the particle diameter range was mainly concentrated between 1.0×10^{-05} and 3.0×10^{-05}, which was mainly distributed around the outlet of the liquid pipe and was radial. From Figure 10b, it can be found that the particle diameter distribution range was 8 μm~40 μm when the outlet of the liquid guide tube was r = 0.36 mm. Among them, the particles with a particle diameter of 8 μm~28 μm accounted for the majority (about 90%), and a small part of the particle diameter distribution was between 28 μm and ~40 μm. When the outlet of the liquid guide tube was a 1 mm × 0.2 mm rectangle, the particle diameter distribution range was 4 μm~24 μm, among which the particles with a particle diameter between 4 μm and ~16 μm accounted for the majority (about 90%), and a small part of the particle diameter distribution was between 16 μm and ~24 μm. When the outlet of the liquid guide tube was 1 mm × 0.4 mm rectangular, the particle diameter distribution range was 8 μm~32 μm, of which the particles between 8 μm and ~24 μm accounted for the majority (about 90%), and a small part of the particle diameter distribution was between 24 μm and ~32 μm. The particle diameter generated at the outlet of the rectangular liquid guide tube was much smaller than that at the circular outlet, and the smaller the rectangular width, the larger the proportion of particles with a particle diameter range of 4 μm~20 μm. In addition, under the same area, the particle diameter range produced by the shear of the r = 0.36 mm circular outlet was not much different from that of the 1 mm × 0.4 mm rectangular outlet, and most of the particle diameters were less than 20 μm. Therefore, the outlet of the rectangular pipe tended to generate small-diameter particles.

L_1 (mm)	L_2 (mm)	d (mm)	D (mm)	X (mm)	Medium	V_1 (m/s)	V_2 (m/s)	Outlet Shape of Guide Pipe	Adaptive Mesh (μm)
2	2.5	1	4	23	100% Ar	498.25	1	1 mm × 0.2 mm rectangle	10
2	2.5	1	4	23	100% Ar	498.25	1	1 mm × 0.4 mm rectangle	10
2	2.5	0.72	4	23	100% Ar	498.25	1	r = 0.36 mm circle	10

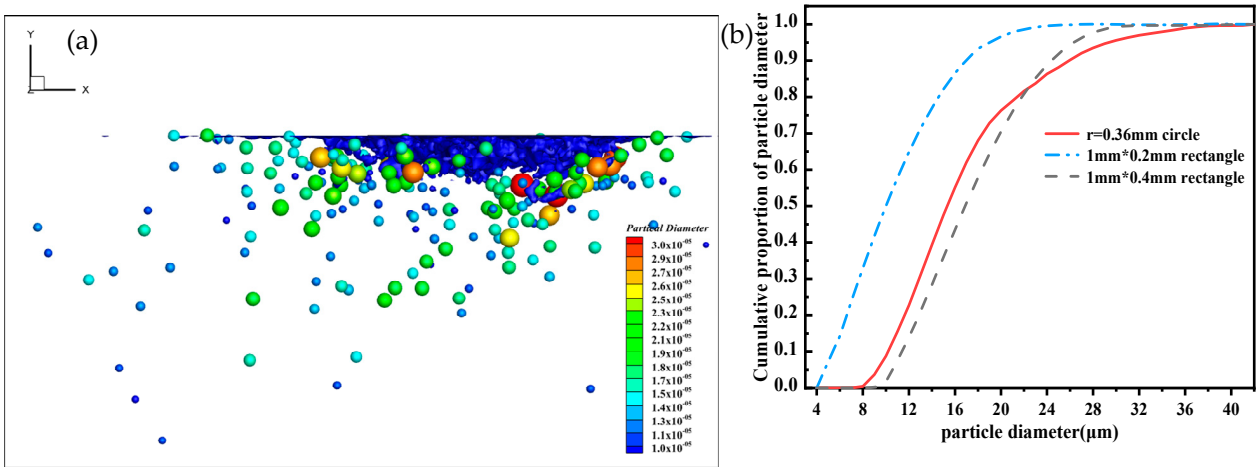

Figure 10. (**a**) Spatial distribution of liquid particles. (**b**) Particle diameter distribution curve.

Figure 11 shows the velocity distribution cloud diagram and vector diagram of the outlet and nearby area of the pipe under different cross-section shapes of the pipe outlet. It can be seen from Figure 11 that the outlet velocity of the fluid at the bottom of the pipe was below 50 m/s, and the velocity of the fluid at the circular outlet was lower. When the outlet section was circular, the lower velocity was not conducive to the collision between the gas and liquid, which led to a decrease in the atomization effect of liquid Cu. In the

third column of Figure 12, the dU/dY velocity gradient of the XY section is very sparse. The liquid Cu flow rate per unit time was constant, and the cross-sectional area of the liquid pipe outlet was reduced, resulting in an increase in the liquid Cu outlet speed. The high-speed flow of plasma moment gas hit the liquid Cu in the horizontal direction, prompting the liquid Cu to break and shear atomization. From the gradient map of Figures 12 and 13, it can be seen that when r = 0.36 mm for the circular outlet, the dU/dY velocity gradient was very sparse and not obvious, the dU/dZ velocity gradient was very dense, and the velocity gradient distribution in both directions was not uniform, so it was not conducive to the shear fragmentation of liquid phase fluid to form particles. In the rectangular section of the outlet of the liquid pipe, it can be seen that with the decrease in the rectangular width, the velocity gradient of dU/dY and dU/dZ gradually became dense, so the decrease in the width of the rectangular outlet was beneficial to the shear fracture of the liquid phase fluid.

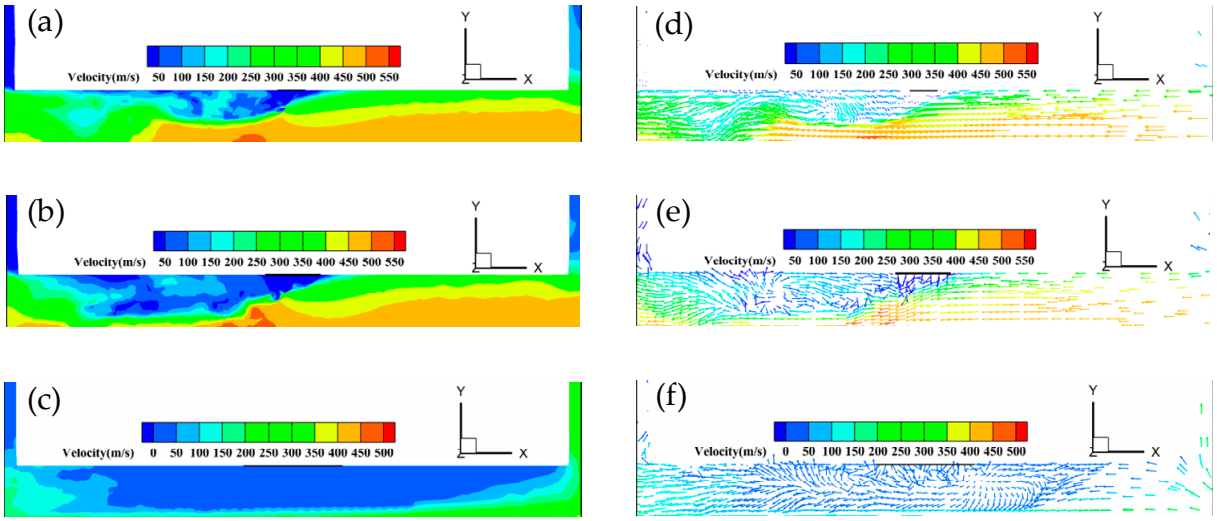

Figure 11. (**a**,**d**), (**b**,**e**), (**c**,**f**) The velocity nephogram and velocity distribution vector diagram when the outlet shape of the pipe was the 1 mm × 0.2 mm rectangle (first row), 1 mm × 0.4 mm rectangle (second row), and r = 0.36 mm circle (third row), respectively.

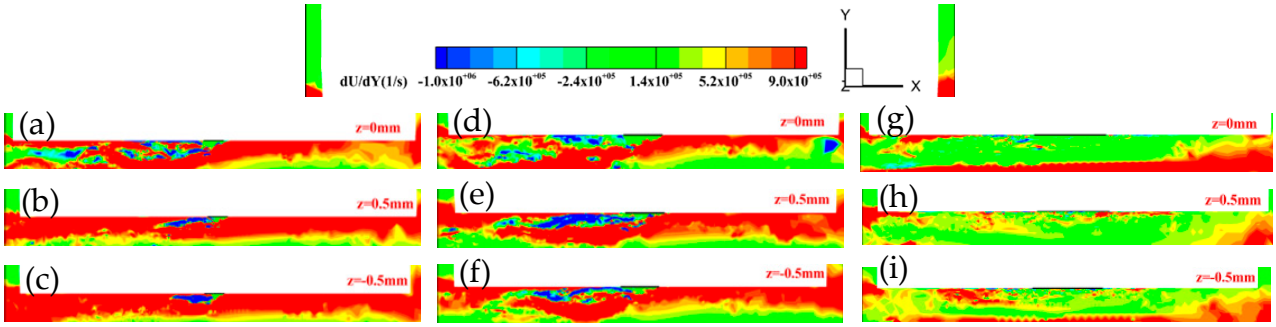

Figure 12. (**a**–**c**) For the 1 mm × 0.2 mm rectangle (first column) X-direction velocity on the Y-axis of the gradient cloud; similarly, (**d**–**f**) for the 1 mm*0.4 mm rectangle (second column) and (**g**–**i**) for the r = 0.36 mm circle (third column).

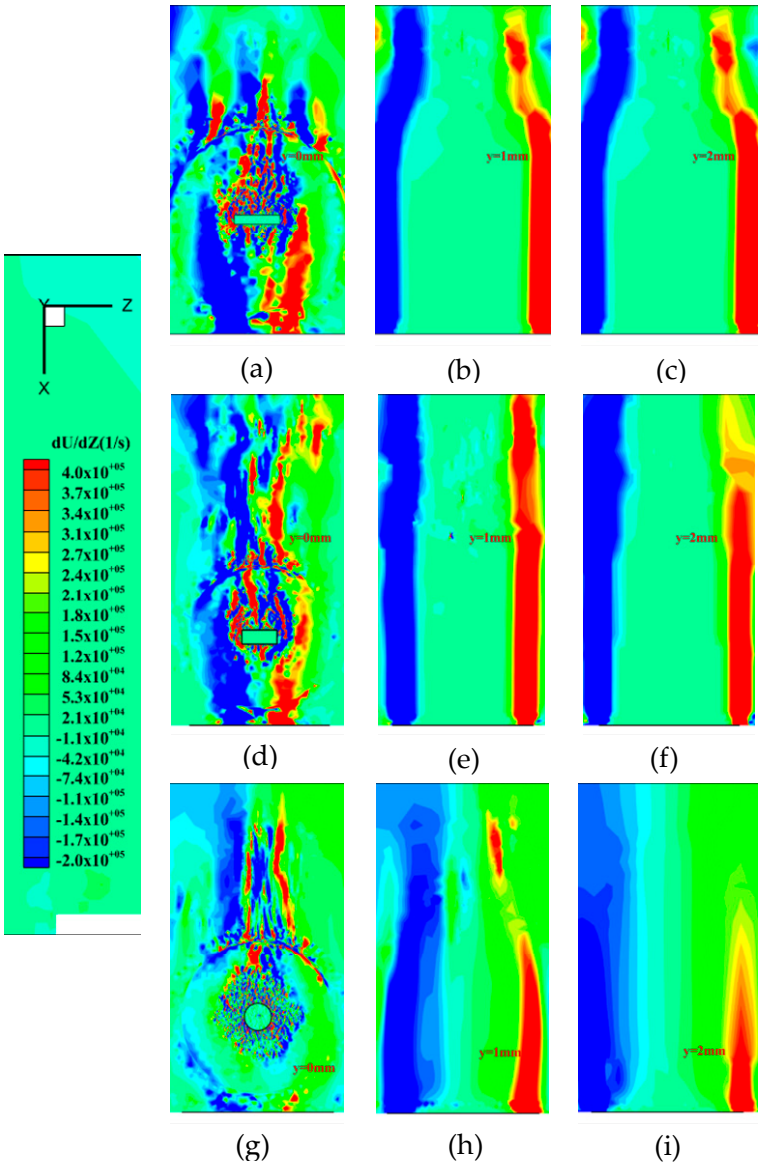

Figure 13. (**a**–**c**) The gradient cloud diagram of the velocity in the X-direction on the Y-axis for the 1 mm × 0.2 mm rectangle (first row); similarly, (**d**–**f**) for the 1 mm × 0.4 mm rectangle (second row) and (**g**–**i**) for r = 0.36 mm circle (third row).

5.3. Surface Tension, σ

Next, the influence of different surface tensions on particle distribution and particle size was analyzed. The aerodynamic force required by the gas-assisted atomization method is generally large. The Weber number represents the ratio of the destruction of aerodynamic force to the recovery of surface tension. It is a very important dimensionless number in evaluating the droplet breakup mode. We studied the effect of the single variable of surface tension from 0.074 N/m to 0.74 N/m on the atomization effect. It can be seen from Figure 14a that the particle phase formed by the shear breakage of the liquid Cu at the outlet of the liquid pipe was mainly distributed on the left and right sides of the outlet of the liquid pipe, and the particle size range was 1.0×10^{-05}~4.0×10^{-05}. It is shown by Figure 14b under this condition. When the surface tension σ = 0.74 N/m, the particle diameter distribution range was 8 μm~44 μm, of which the particles with a particle diameter between 8 μm and ~28 μm accounted for the vast majority (about 90%), and a small part of the particle size was distributed between 28 μm and ~44 μm. When the surface tension σ = 0.074 N/m, the particle diameter distribution range was 9 μm~44 μm,

of which the particles between 9 μm and ~28 μm accounted for the majority (about 90%), and a small part of the particle diameter distribution was between 28 μm and ~44 μm. The surface tension of the liquid prevents the development of the liquid film to form droplets. With the increase in the surface tension, the liquid Cu with large surface tension dissipated more work, which consumed too much atomization energy, so the energy of liquid atomization was relatively less, which was not enough to form small droplets. Under the same atomization pressure, the cumulative proportion of particle size distribution of liquid Cu atomized particles with large surface tension tended toward 1 slowly; that is, the atomization effect was relatively poor. It can be seen that the surface tension of the liquid had an inhibitory effect on the development of the liquid film. Therefore, small surface tension tended toward the formation of small-diameter particles.

L_1 (mm)	L_2 (mm)	d (mm)	D (mm)	X (mm)	Medium	V_1 (m/s)	σ (N/m)	V_2 (m/s)	Outlet Shape of Guide Pipe	Adaptive Mesh (μm)
2	2.5	1	4	23	100% Ar	498.25	0.074	1	1 mm × 0.4 mm rectangle	10
2	2.5	1	4	23	100% Ar	498.25	0.74	1	1 mm × 0.4 mm rectangle	10

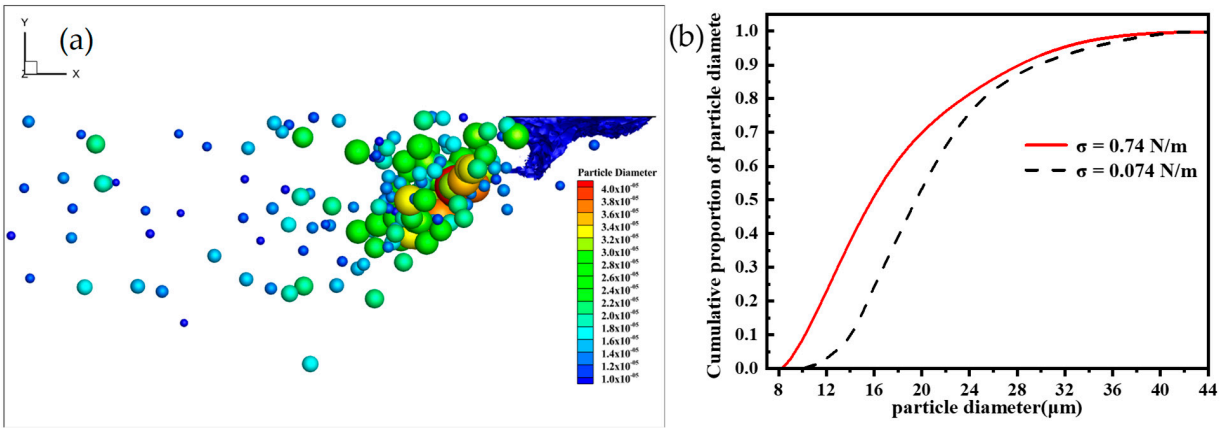

Figure 14. (**a**) Spatial distribution of liquid particles. (**b**) Particle size distribution curve.

Figure 15 shows the velocity distribution cloud diagram and velocity vector diagram of the outlet and nearby area of the liquid pipe under the conditions of surface tension σ = 0.074 N/m and σ = 0.74 N/m. It can be seen from Figure 15 that the outlet velocity of the fluid at the bottom of the liquid pipe with two kinds of surface tension was below 50 m/s, and the difference was not significant. The surface tension was due to the interaction between molecules in the thin layer of the liquid surface. The larger the surface tension was, the slower the liquid Cu flowed out from the outlet of the liquid pipe. The lower speed was not conducive to the collision between the gas and liquid, resulting in a decrease in the atomization effect of the liquid Cu. In Figures 16 and 17, the gradient maps show that when the surface tension σ = 0.74 N/m, the velocity gradient in the two directions of dU/dY and dU/dZ became sparse. Compared with σ = 0.074 N/m, it can be found that with the increase in surface tension, the velocity gradient of dU/dY and dU/dZ gradually became sparse, so the increase in surface tension was not conducive to the shear fragmentation of the liquid Cu.

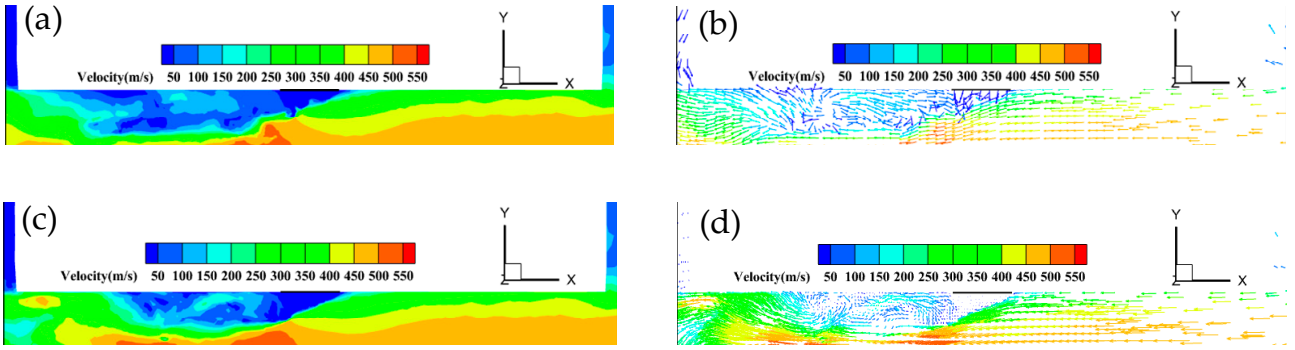

Figure 15. (**a**,**b**), (**c**,**d**) The velocity nephogram and velocity distribution vector diagram when the surface tension σ = 0.074 (first row) and σ = 0.74 (second row), respectively.

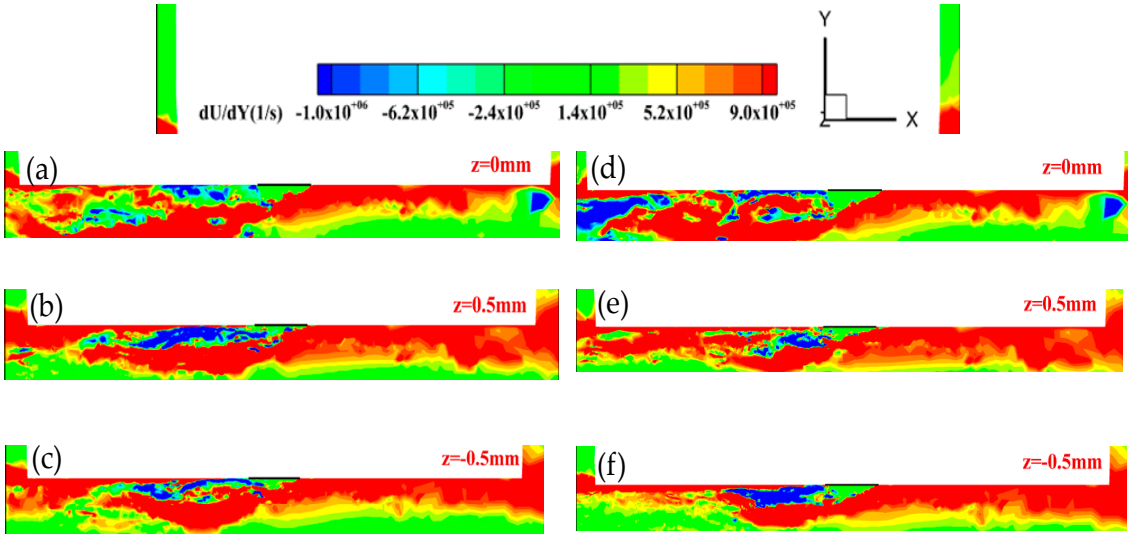

Figure 16. (**a**–**c**) The gradient contours of the velocity in the X-direction of the surface tension σ = 0.074 (first column) on the Y-axis, and similarly (**d**–**f**) for σ = 0.74 (second column).

5.4. Collection Tube Length, L

Next, the influence of the length of the collection tube on the particle distribution and particle size was analyzed. We studied the effect of collection tube lengths L = 0 mm and L = 40 mm on the atomization effect. It can be seen from Figure 18a that the particle phase formed by the shear breakage of the liquid Cu at the outlet of the liquid pipe was mainly distributed on the left and right sides of the outlet of the liquid pipe, and the particle size range was 9.0×10^{-06}~2.6×10^{-05}. As shown in Figure 18b, under this working condition, the particle diameter distribution range formed when the length of the collection tube L = 40 mm was 8 μm~24 μm, of which the particles with a particle diameter between 8 μm and ~18 μm accounted for the vast majority (about 90%), and a small part of the particle diameter was distributed between 18 μm and ~24 μm. When the length of the collection tube was L = 0 mm, the particle diameter distribution range was 9 μm~44 μm, of which the particles with a particle diameter between 9 μm and ~28 μm accounted for the vast majority (about 90%), and a small part of the particle size was distributed between 28 μm and ~44 μm. The reason is that the extension length of the collection tube had a great influence on the particle size of the powder. The constraint structure of the collection tube was added, which concentrated the airflow at the gas nozzle of the plasma torch, the effective atomization airflow pressure was large, so the liquid Cu was quickly atomized and broken to form small droplets, and the average particle size was small. It can be seen that the constraint structure of increasing the collection tube had a promoting effect on the

shear atomization of the liquid film. Therefore, the collection tube length L = 40 mm will tend toward the formation of small particles.

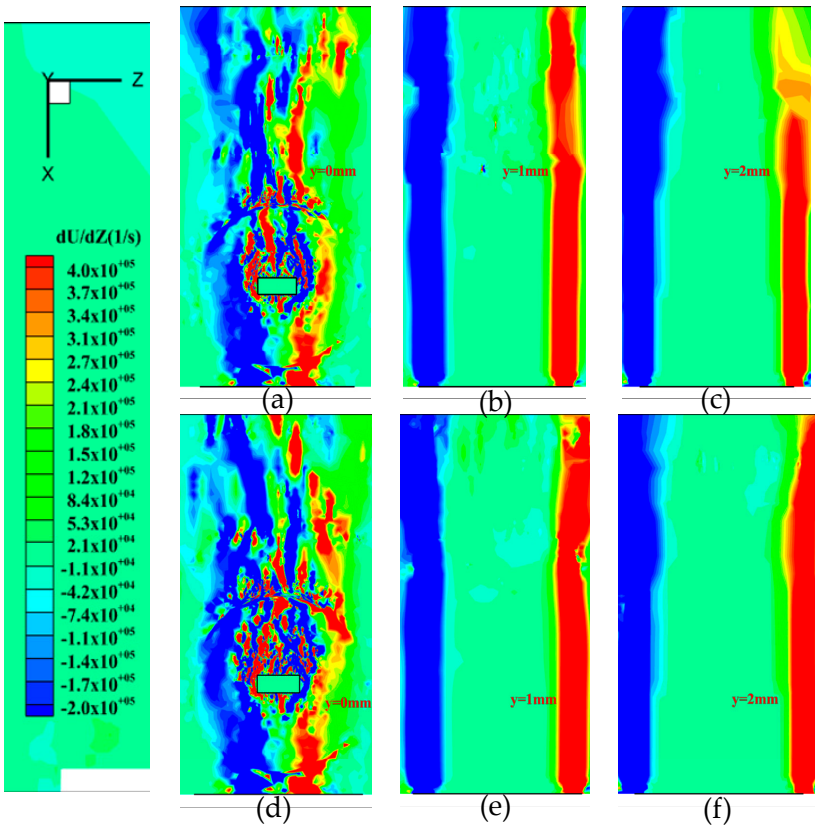

Figure 17. (**a**–**c**) The gradient contours of the velocity in the X-direction of the surface tension σ = 0.074 (first row) on the Z-axis, and similarly (**d**–**f**) for σ = 0.74 (second row).

L_1 (mm)	L_2 (mm)	d (mm)	D (mm)	X (mm)	Medium	L (mm)	V_2 (m/s)	Outlet Shape of Guide Pipe	Adaptive Mesh (μm)
2	2.5	1	4	23	100% Ar	0	1	1 mm × 0.4 mm rectangle	10
2	2.5	1	4	23	100% Ar	40	1	1 mm × 0.4 mm rectangle	10

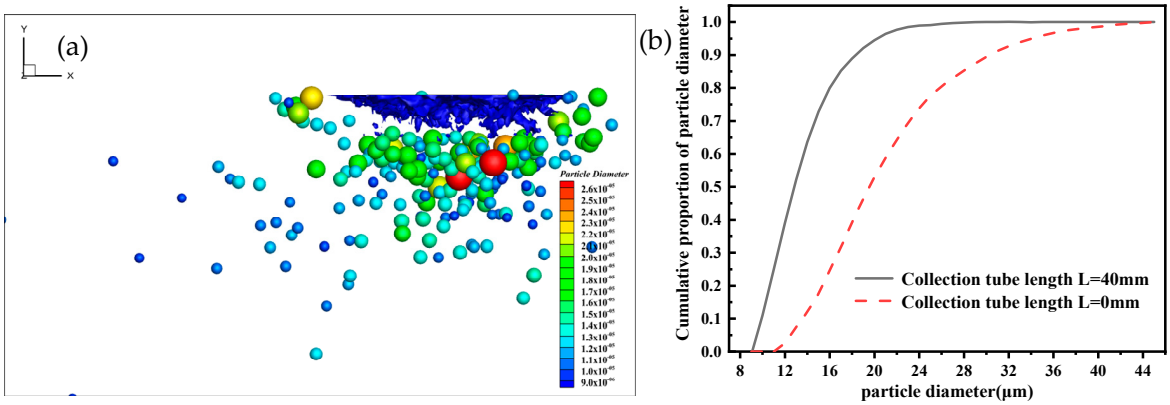

Figure 18. (**a**) Spatial distribution of liquid particles. (**b**) Particle size distribution curve.

From the velocity contours in Figure 19a,c, it can be seen that the outlet velocity of the fluid at the bottom of the liquid pipeline was below 50 m/s, while the velocity below the outlet of the liquid pipe was between 400 and ~550 m/s when there was no collection tube, and the velocity below the outlet of the liquid pipe was less than 400 m/s after increasing the length of the collection tube, L = 40 mm. From the velocity vector distribution of the flow field, it can be seen that when the length of the collection tube was L = 0 mm, at the XY section, the flow direction of the fluid gradually changed from longitudinal to transverse, forming a vortex, and the length of the collection tube was L = 40 mm. Under the constraint structure of the collection tube, the plasma torch gas flow was concentrated and flowed horizontally. It is well known that there is a velocity difference between the liquid pipeline fluid and the plasma momentum gas, and the liquid fluid will undergo shear fragmentation. Therefore, the constraint structure of the collection tube was added, and the airflow was concentrated, so the liquid phase fluid was broken into particle phase in time by greater shear action, as shown in Figures 20 and 21 in the dU/dY and dU/dZ gradient maps. In Figure 20, from left to right, the velocity gradient is gradually dense, and Figure 21 is dense from top to bottom.

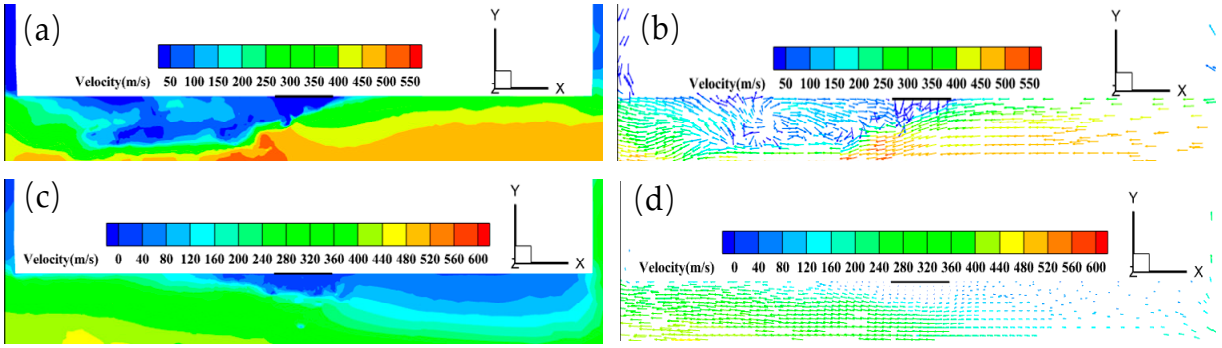

Figure 19. (**a**,**b**), (**c**,**d**) The velocity nephogram and velocity distribution vector diagram when the collection tube length L = 0 mm (first row) and L = 40 mm (second row), respectively.

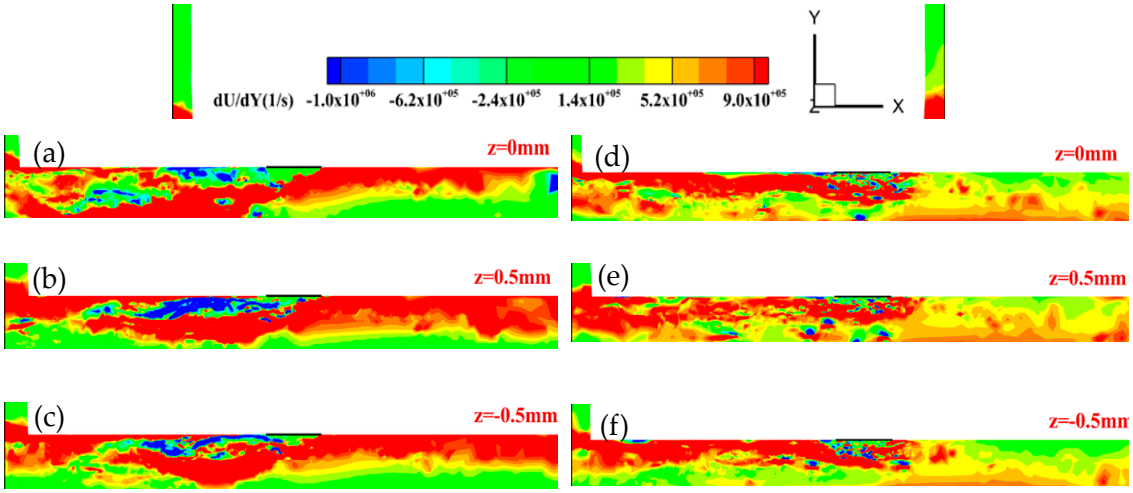

Figure 20. (**a**–**c**) The gradient cloud images of the velocity in the X-direction on the Y-axis with the length of the collection tube L = 0 mm (first column), and (**d**–**f**) are the gradient cloud images of L = 40 mm (second column).

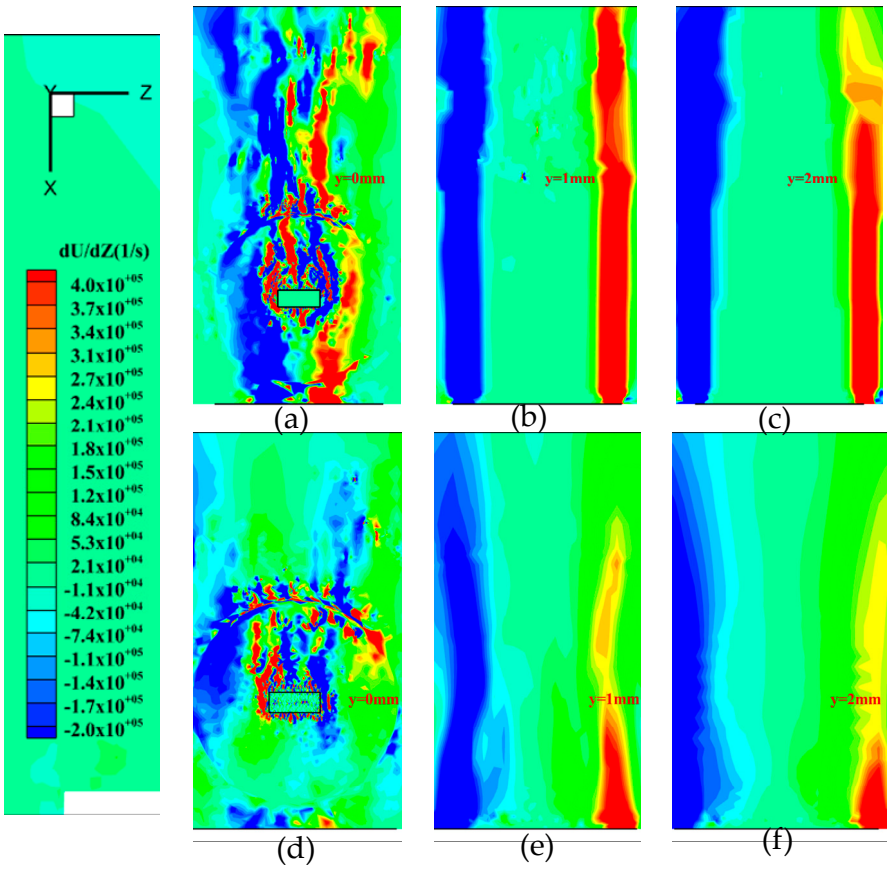

Figure 21. (**a**–**c**) The gradient cloud images of the velocity on the Z-axis in the X-direction of the length of the collection tube L = 0 mm (first row), and (**d**–**f**) are the gradient cloud images of L = 40 mm (second row).

5.5. Increasing the Angle of Chamfer at the Outlet of the Guide Pipe

When the outlet of the guide pipe increased the angle of chamfer, it can be seen that it had a great influence on the particle diameter range. It can be seen from Figure 22a that the particle phase formed by the shear breakage of liquid Cu at the outlet of the guide pipe was mainly distributed around the outlet of the liquid pipe, and the particle diameter range was 1.0×10^{-05}~3.0×10^{-05}. Figure 22b shows that under this condition, when the chamfer was added to the outlet of the pipe, the particle diameter distribution range was 8 μm~30 μm, of which the particles with a particle diameter between 8 μm and ~20 μm accounted for the vast majority (about 90%), and a small part of the particle diameter distribution was between 20 μm and ~30 μm. When the outlet of the liquid guide tube was at a right angle, the particle diameter distribution range was 9 μm~44 μm, in which the particles between 9 μm and ~28 μm accounted for the vast majority (about 90%), and a small part of the particle diameter distribution was between 28 μm and ~44 μm. The chamfering treatment reduced the overall resistance of the transverse flow of the plasma torch gas, intensified the shear movement, and weakened the vortex strength, so the plasma torch gas and liquid Cu were fully mixed and sheared, and the atomization effect was relatively better. Therefore, after chamfering treatment, it was more conducive to the formation of small particles.

L_1 (mm)	L_2 (mm)	d (mm)	D (mm)	X (mm)	Medium	V_1 (m/s)	V_2 (m/s)	Outlet Shape of Guide Pipe	Adaptive Mesh (μm)
2	2.5	1	4	23	100% Ar	498.25	1	right angle	10
2	2.5	1	4	23	100% Ar	498.25	1	chamfer	10

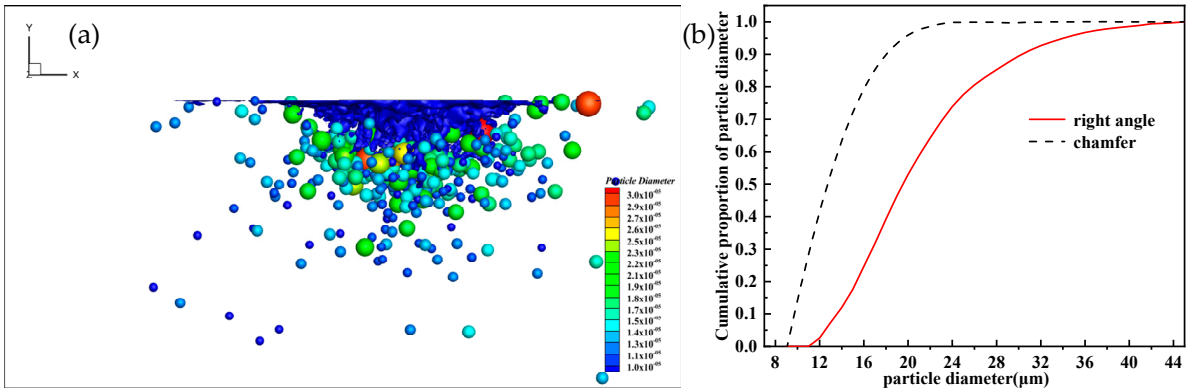

Figure 22. (**a**) Spatial distribution of liquid particles. (**b**) Particle diameter distribution curve.

From the velocity contours in Figure 23a,c, it can be seen that the outlet velocity of the fluid at the bottom of the liquid guide tube was lower than 50 m/s, and the outlet velocity was lower after the chamfering was added. The reason is that the chamfering treatment shrunk the nozzle of the liquid guide tube, and the flow of liquid Cu was buffered. According to the velocity vector distribution diagram, it can be concluded that at the same plasma torch gas flow rate, when the outlet of the guide pipe was at a right angle, in the XY section, the flow direction of the fluid at the outlet of the liquid guide tube changed from vertical to transverse, forming an eddy current. When chamfered, the transverse flow resistance of the plasma torch gas decreased, and no eddy current was formed with the fluid at the outlet of the liquid guide tube. The chamfering treatment reduced the lateral flow resistance of the plasma torch gas, so it was fully mixed and sheared with the liquid Cu flowing out of the liquid pipe, and the liquid Cu was broken into the particle phase more thoroughly. Therefore, as shown in Figures 24 and 25, the dU/dY velocity gradient of Figure 24 gradually became dense from left to right, and the dU/dZ velocity gradient of Figure 25 gradually became dense from top to bottom.

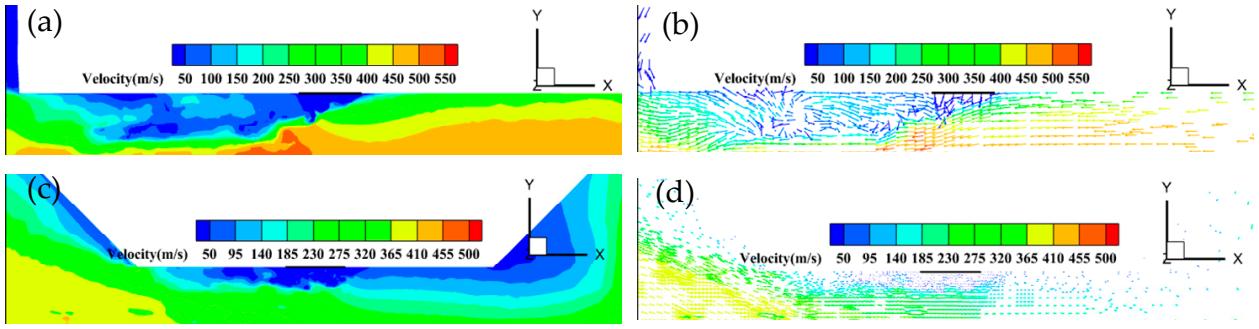

Figure 23. (**a**,**b**), (**c**,**d**) The velocity nephogram and velocity distribution vector diagram when the right angle was used (first row) and when the chamfer was added to the outlet of the guide pipe (second row), respectively.

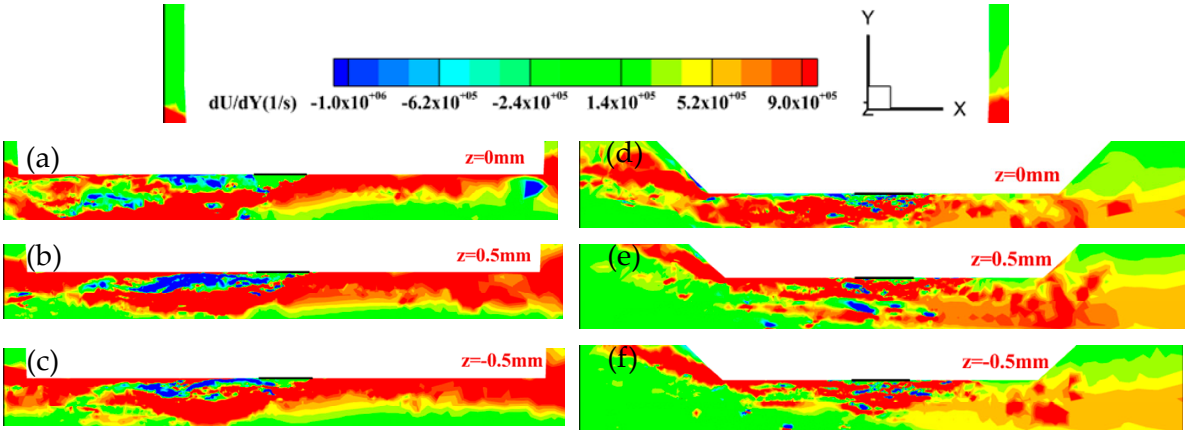

Figure 24. (**a**–**c**) The gradient contours of the velocity in the X-direction for the outlet of the guide pipe at the right angle (first column) on the Y-axis, and similarly (**d**–**f**) for the chamfer (second column).

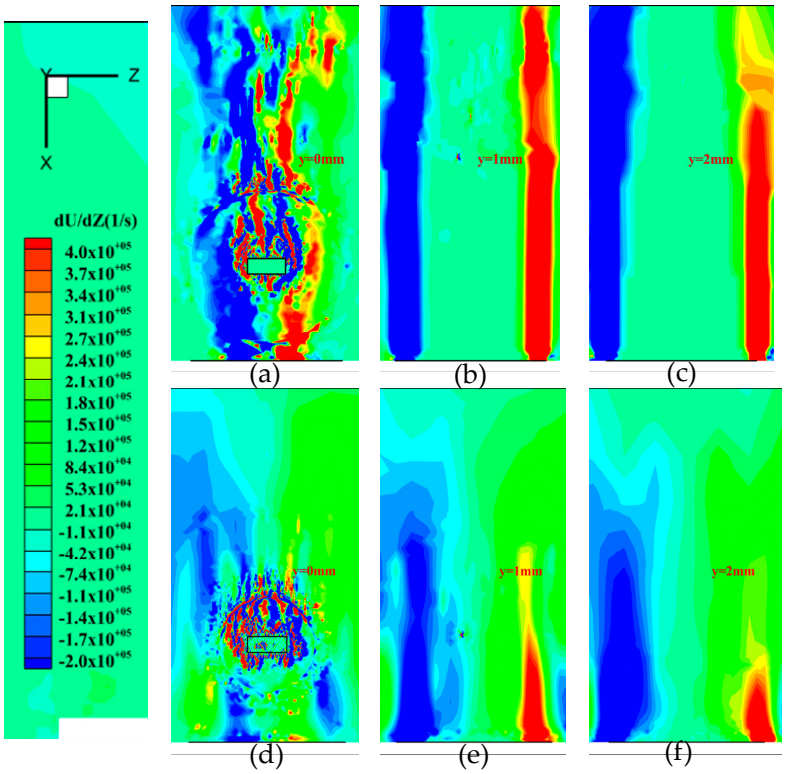

Figure 25. (**a**–**c**) The gradient contours of the velocity in the X-direction for the outlet of the guide pipe at the right angle (first row) on the Z-axis, and similarly (**d**–**f**) for the chamfer (second row).

5.6. The Vertical Distance from the End of the Liquid Tube to the Center of the Plasma Torch Outlet, L_1

Finally, the influence of the vertical distance L_1 from the end of the liquid pipe to the center of the plasma torch outlet on the particle size range of the liquid Cu shear broken into particle phase was analyzed. It can be seen from Figure 26a that the particles of shear atomization at the outlet of the liquid pipe were mainly distributed near the outlet of the liquid pipe, and the particle size range was 8.0×10^{-06}~3.0×10^{-05}. From Figure 26b, under this working condition, when the vertical distance from the end of the liquid guide tube to the center of the plasma torch outlet was $L_1 = 0$ mm, the particle diameter distribution range was 8 μm~36 μm, of which the particles with a particle diameter between 8 μm and ~22 μm accounted for the vast majority (about 90%), and a small part of the particle diameter

distribution was between 22 μm and ~36 μm. When L_1 = 1 mm, the particle diameter distribution range was 8 μm~51 μm, of which the particles with a particle diameter between 8 μm and ~28 μm accounted for the vast majority (about 90%), and a small part of the particle diameter distribution was between 28 μm and ~51 μm. When L_1 = 2 mm, the particle diameter distribution range was 8 μm~45 μm, of which the particles with a particle diameter between 8 μm and ~30 μm accounted for the vast majority (about 90%), and a small part of the particle diameter distribution was between 30 μm and ~45 μm. The vertical distance L_1 from the end of the liquid guide tube to the center of the plasma torch outlet had a great influence on the particle diameter of the powder. The possible reason is that, as the end of the liquid guide tube was close to the center of the plasma torch, at the same plasma torch gas flow rate V_1, the closer the end of the liquid guide tube was, the stronger the plasma torch gas shear effect was, so the liquid Cu was rapidly sheared and broken into particles. Meanwhile, the farther the end of the liquid guide tube was, the weaker the plasma torch gas shear effect was, resulting in an atomization effect of liquid Cu that was not as good as the former. Therefore, the decrease in the vertical distance L_1 from the end of the liquid guide tube to the center of the plasma torch outlet tended toward the formation of small-diameter particles.

L_1 (mm)	L_2 (mm)	d (mm)	D (mm)	X (mm)	Medium	V_1 (m/s)	V_2 (m/s)	Outlet Shape of Guide Pipe	Adaptive Mesh (μm)
0	2.5	1	4	23	100% Ar	498.25	1	1 mm × 0.4 mm rectangle	10
1	2.5	1	4	23	100% Ar	498.25	1	1 mm × 0.4 mm rectangle	10
2	2.5	1	4	23	100% Ar	498.25	1	1 mm × 0.4 mm rectangle	10

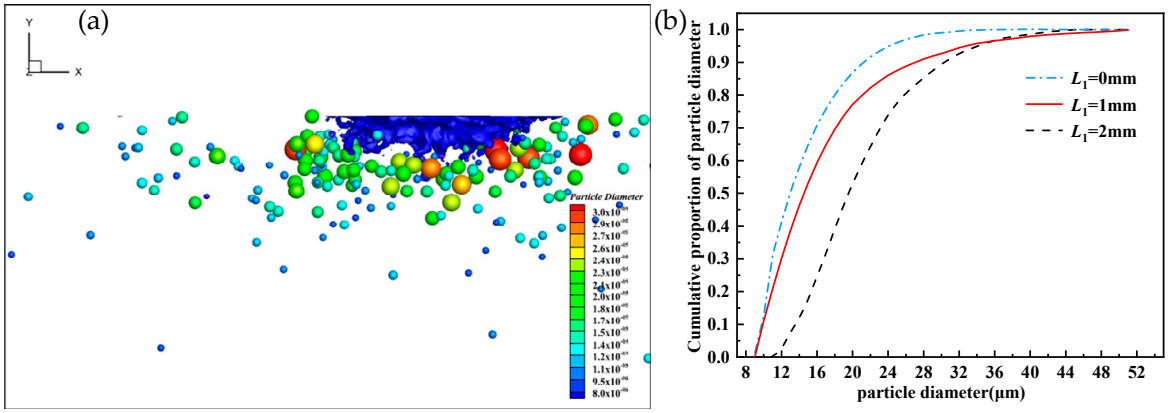

Figure 26. (**a**) Spatial distribution of liquid particles. (**b**) Particle size distribution curve.

From the velocity contours in Figure 27a–c, it can be seen that the outlet velocity of the fluid at the bottom of the pipe was below 50 m/s, but when L_1 = 0 mm, the bottom of the pipe was close to the center of the plasma torch, and the transverse velocity of the plasma torch was large and dense, which occupied a dominant position. It can be seen from the XY section that the fluid at the outlet of the pipe was sheared, and the flow direction changed from longitudinal to transverse, forming a vortex. With the increase in L_1, the bottom of the liquid guide tube was far away from the center of the plasma torch. When L_1 = 1 mm, the effect of shearing the fluid at the outlet of the liquid guide tube was weakened, and when L_1 = 2 mm, the fluid flow direction of the liquid guide tube changed from longitudinal to transverse. The proportion was less, because the smaller the vertical distance between the end of the liquid guide tube and the center of the plasma torch, the stronger the liquid Cu

was sheared and broken by the plasma torch gas, and it was broken into a granular phase in time and no large liquid phase was generated. As shown in Figures 28 and 29 in the dU/dY and dU/dZ gradient maps, the velocity gradient of Figure 28 was gradually dense from left to right, and the velocity gradient of Figure 29 was gradually dense from top to bottom. It can be seen that the smaller the L_1 value, the better the shear effect of the liquid phase fluid. Therefore, the decrease in the L_1 value of the vertical distance between the end of the liquid guide tube and the center of the plasma torch was beneficial to the shear fragmentation of the liquid phase fluid.

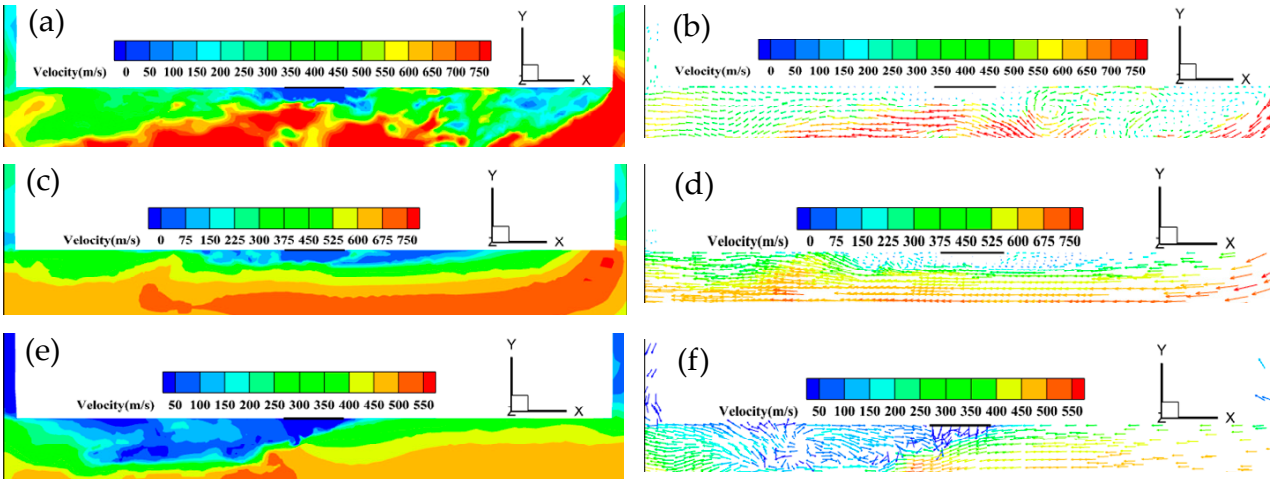

Figure 27. (**a**,**d**), (**b**,**e**), (**c**,**f**) The velocity nephogram and velocity distribution vector diagram when L_1 = 0 mm (first row), L_1 = 1 mm (second row), and L_1 = 2 mm (third row), respectively.

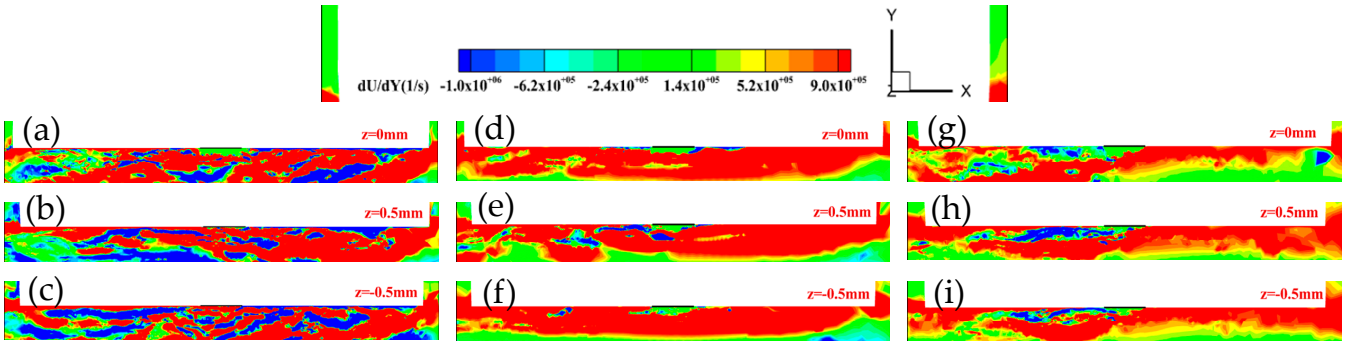

Figure 28. (**a**–**c**) For L_1 = 0 mm (first column), X-direction velocity on the Y-axis of the gradient cloud, and similarly for (**d**–**f**) L_1 = 1 mm (second column) and (**g**–**i**) L_1 = 2 mm (third column).

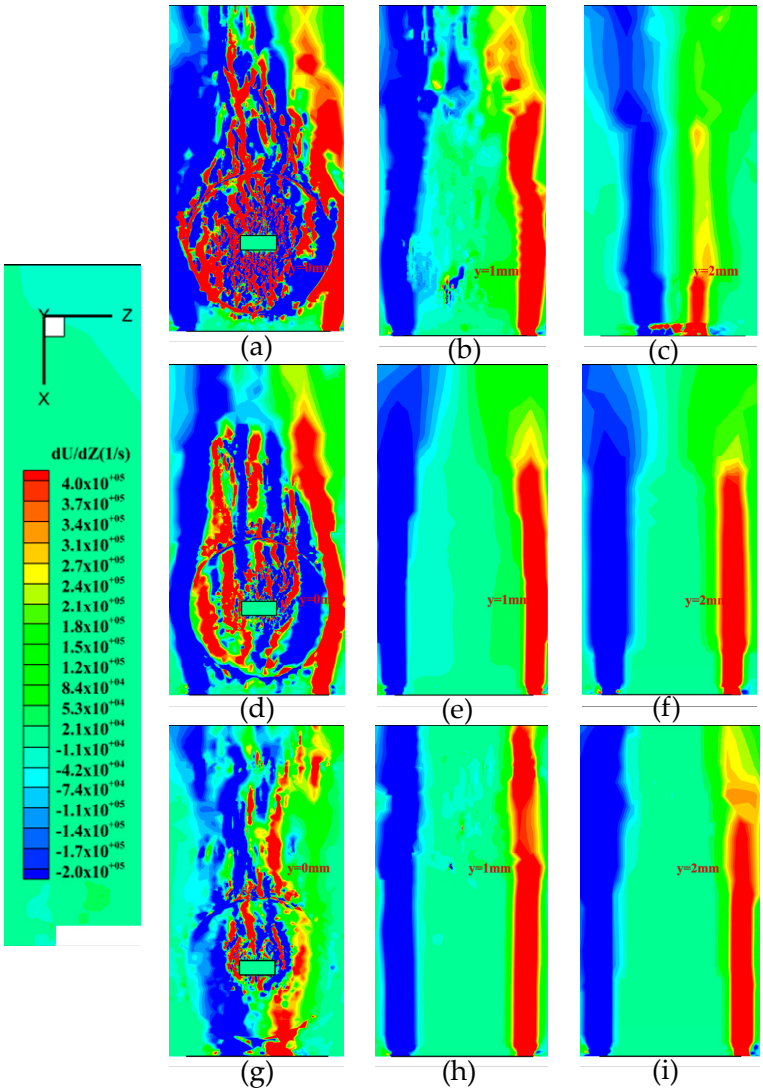

Figure 29. (**a**–**c**) The gradient cloud diagram of the velocity in the X-direction on the Y-axis when L_1 = 0 mm (first row); similarly, (**d**–**f**) L_1 = 1 mm (second row) and (**g**–**i**) L_1 = 2 mm (third row).

6. Conclusions

Based on the observation of experimental phenomena and numerical simulation analysis, in this paper, we mainly studied the non-stationary simulation of the DC argon plasma torch, analyzed the specific influence law of the average particle diameter of the powder in the plasma atomization process, established the mapping relationship between the atomization conditions and the average particle diameter of the powder, and proposed the powder quality control scheme. The experimental verification of the theoretical model was carried out by using industrial-grade plasma atomization equipment. The relevant results and conclusions can provide production guidance for plasma atomization and promote the development of the plasma atomization process. The main research results and conclusions are summarized as follows:

(1) In this study, based on the dynamic adaptive grid method, the VOF to DPM coupling model and the KH-RT fragmentation model were used to simulate the atomization process of the high-temperature plasma torch high-speed jet impinging on liquid Cu. It was found that under the impact of the plasma jet, liquid Cu first formed an irregular liquid column, and the edge of the liquid column was further sheared and broken to form an irregular liquid block. The liquid block was removed from the VOF model and appeared in the form of particle phase in the DPM; that is, the

irregular liquid block further condensed under the interfacial tension to form broken droplet particles.

(2) Based on the industrial plasma atomization equipment, the theoretical model proposed in this paper was verified. Based on experimental observation and numerical simulation, the following research findings and results were obtained: Based on the industrial plasma atomization equipment, the powder preparation experiment of optimizing the average particle diameter of the powder was carried out, and the reliability of the theoretical model was verified. The powder with a dimensionless particle diameter less than 0.84 μm was prepared under the low-power conditions of a plasma generator Ar flow rate of 14.4 m^3/h, current of 149 A, voltage of 63 V, and power of 9.4 kW. The variation law of the calculated value of the dimensionless particle diameter of the powder in the experimental group was basically consistent with the simulated value, and the maximum relative error between the two was 0.069.

(3) A powder-quality-control scheme based on industrial-grade plasma atomization equipment was proposed. It was mainly for the control of the average particle diameter of the powder and the width of the particle diameter distribution. (1) Based on the average particle diameter calculation model, the average particle diameter value could be predicted after the process parameters were changed. In particular, the larger the gas flow rate of the plasma moment or the rectangular outlet of the liquid guide tube, the smaller the average particle diameter of the powder. (2) For powder particle diameter distribution width control, increasing the collection tube constraint at the plasma torque outlet, or chamfering the outlet of the liquid guide tube, effectively reduced the particle diameter distribution width of the powder.

Author Contributions: Methodology, F.X.; Writing—original draft, T.L.; Supervision, G.X. and G.C.; Project administration, X.L. All authors have read and agreed to the published version of the manuscript.

Funding: This research was funded by Zhejiang Provincial Natural Science Foundation of China (No. LQ21A020007) And the APC was funded by Ningbo Guangxin Nanomaterials Ltd.

Data Availability Statement: The original contributions presented in the study are included in the article, further inquiries can be directed to the corresponding author.

Conflicts of Interest: The authors declare that this study received funding from Ningbo Guangxin Nanomaterials Ltd. The funder had the following involvement with the study: The plasma atomization pulverizing experiment of this study was completed in Ningbo Guangxin Nanomaterials Ltd., and the enterprise provided experimental data and technical support.

References

1. Korzhyk, V.; Strohonov, D.; Burlachenko, O.; Voitenko, O.; Kunitskyi, D. Development of plasma-arc technologies of spherical granule production for additive manufacturing and granule metallurgy. *Paton Weld. J.* **2023**, *12*, 3–18. [CrossRef]
2. Wang, P.; Li, J.; Wang, X.; Du, B.R.; Shen, S.Y.; Ge, X.Y.; Wang, M.H. Impact mechanism of gas temperature in metal powder production via gas atomization. *Chin. Phys. B* **2021**, *30*, 054702. [CrossRef]
3. Wu, C.-J.; Cheng, S.-L.; Sheng, Y.-J.; Tsao, H.-K. Reduction-assisted sintering of micron-sized copper powders at low temperature by ethanol vapor. *RSC Adv.* **2015**, *5*, 53275–53279. [CrossRef]
4. Wu, S.; Meng, S. Preparation of micron size copper powder with chemical reduction method. *Mater. Lett.* **2006**, *60*, 2438–2442.
5. Ranjana, M.; Sahu, P.; Ramesh, V.V.E.; Kumar, A.K.N.; Babu, T.G.S.; Kumar, D.V.R. Ethylenediamine Mediated, Environmentally Benign Synthesis of Copper Nanowires and their Catalytic Activity towards 4-Nitrophenol Reduction. *Chemistryselect* **2023**, *8*, e202204351. [CrossRef]
6. Fong, Y.M.M. Development of Copper Nanocomposite Coatings for All-Optical Ultrasound Bioimaging. Ph.D. Thesis, University College London, London, UK, 2023.
7. Ziemkiewicz, D.; Zielinska-Raczynska, S. Copper plasmonics with excitons. *Phys. Rev. B* **2022**, *106*, 205404. [CrossRef]
8. Jalilian, Z.; Moradian, R. The substrate effect on optical response of plasmonic metamaterials. *J. Mater. Sci. Mater. Electron.* **2022**, *33*, 19839–19845. [CrossRef]
9. Yang, Y.; Wang, S.X.; He, W.; Hu, K.; He, B.; Mo, Y.Q. Preparation of Ultra-Fine Copper Powder and Its Application in Manufacturing Conductive Lines by Printed Electronics Technology. In Proceedings of the International Conference on Applied Superconductivity and Electromagnetic Devices, Chengdu, China, 25–27 September 2009.

10. Krasnov, A. Plasma atomization of tungsten. *Sov. Powder Metall. Met. Ceram.* **1966**, *5*, 79–83. [CrossRef]
11. Wang, M.R.; Chen, P.J. Mechanism and Performance of a Novel Supersonic Atomizer for Metal Powder Production. *J. Chin. Soc. Mech. Eng.* **2016**, *37*, 435–440.
12. Liu, L.L.; Zhang, J.L.; Zhang, Q.; Zhai, C.S.; Zheng, H.X. Computational insights into gas atomization of FeCoNiCrMoBSi high-entropy alloy: From droplet formation to rapid solidification. *Int. J. Heat Mass Transf.* **2024**, *228*, 125628. [CrossRef]
13. Garboczi, E.; Hrabe, N. Particle shape and size analysis for metal powders used for additive manufacturing: Technique description and application to two gas-atomized and plasma-atomized Ti64 powders. *Addit. Manuf.* **2020**, *31*, 100965. [CrossRef]
14. Entezarian, M.; Allaire, F.; Tsantrizos, P.; Drew, R. Plasma atomization: A new process for the production of fine, spherical powders. *JOM* **1996**, *48*, 53–55. [CrossRef]
15. Entezarian, M. Reactive Plasma Spray Forming of Al-TiAl3 Composites Using a Triple Plasma System. Ph.D. Thesis, McGill University, Montreal, QC, Canada, 1997.
16. Dion, C.A.D.; Kreklewetz, W.; Carabin, P. Plasma Apparatus for the Production of High Quality Spherical Powders at High Capacity. U.S. Patent Application 15/579,693, 21 June 2018.
17. Proulx, F.; Dion, C.A.D.; Carabin, P. Method and Apparatus for Producing High Purity Spherical Metallic Powders at High Production Rates from One or Two Wires. WO 2019/232,612, 12 December 2019.
18. Yin, Z.; Yu, D.; Zhang, Q.; Yang, S.; Yang, T. Experimental and numerical analysis of a reverse-polarity plasma torch for plasma atomization. *Plasma Chem. Plasma Process.* **2021**, *41*, 1471–1495. [CrossRef]
19. Wang, C.; Weng, Z.; Jin, X. Preparation of FGH98 high temperature alloy powder for 3D printing by plasma rotating electrode method. *J. Zhejiang Metall.* **2019**, *2*, 1–3.
20. Tsuji, Y.; Kawaguchi, T.; Tanaka, T. Discrete particle simulation of two-dimensional fluidized bed. *Powder Technol.* **1993**, *77*, 79–87. [CrossRef]
21. Zahari, N.; Zawawi, M.; Sidek, L.M.; Mohamad, D.; Itam, Z.; Ramli, M.; Syamsir, A.; Abas, A.; Rashid, M. Introduction of discrete phase model (DPM) in fluid flow: A review. In *Green Design and Manufacture: Advanced and Emerging Applications, Proceedings of the 4th International Conference on Green Design and Manufacture 2018, Ho Chi Minh, Vietnam, 29–30 April 2018*; AIP Publishing: Melville, NY, USA, 2018.
22. Adam, A.; He, W.; Fan, Y.H.D. Investigation of flow characteristics and mixing of liquid hydrogen within a premixing swirl tube for the turbine engine combustor. *Int. J. Hydrogen Energy* **2024**, *49*, 367–383. [CrossRef]
23. Luo, S.; Wang, H.; Gao, Z.; Wu, Y.; Wang, H. Interaction between high-velocity gas and liquid in gas atomization revealed by a new coupled simulation model. *Mater. Des.* **2021**, *212*, 110264. [CrossRef]
24. Cervone, A.; Manservisi, S.; Scardovelli, R.; Sirotti, L.; Xiao, M.A. Computing Interface Curvature from Height Functions Using Machine Learning with a Symmetry-Preserving Approach for Two-Phase Simulations. *Energies* **2024**, *17*, 3674. [CrossRef]
25. Potyka, J.; Schulte, K. A Volume of Fluid Method for Three Dimensional Direct Numerical Simulations of Immiscible Droplet Collisions. *Int. J. Multiph. Flow* **2024**, *170*, 104654. [CrossRef]
26. Cruz, A.T.; Lange, D.F.D.; Paepegem, W.V. Efficient single variable Level Set method for capturing moving interfaces in powder densification processes. *Comput. Methods Appl. Mech. Eng.* **2024**, *428*, 117086. [CrossRef]
27. Lyras, P.; Hubert, A.; Lyras, K.G. A conservative level set method for liquid–gas flows with application in liquid jet atomisation. *Exp. Comput. Multiph. Flow* **2023**, *5*, 67–83. [CrossRef]
28. Jin, W.; Xiao, J.; Ren, H.; Li, C.; Zheng, Q.; Tong, Z. Three-dimensional simulation of impinging jet atomization of soft mist inhalers using the hybrid VOF-DPM model. *Powder Technol.* **2022**, *407*, 117622. [CrossRef]
29. Liu, C.; Xi, X.; Liu, H.; Li, W.; Jia, M.; Li, R. Multi-Scale methodology of breakup and atomization for liquid jets in crossflow. *Appl. Therm. Eng.* **2024**, *248*, 123309. [CrossRef]
30. Shi, P.; Zhu, G.; Cheng, J.; Li, J.; Hou, X. Simulation on atomization process of gas–liquid pintle injector in LRE under periodic conditions based on the VOF to DPM method. *Aerosp. Sci. Technol.* **2023**, *136*, 108222. [CrossRef]
31. Wei, M.; Chen, S.; Sun, M.; Liang, J.; Liu, C.; Wang, M. Atomization simulation and preparation of 24CrNiMoY alloy steel powder using VIGA technology at high gas pressure. *Powder Technol.* **2020**, *367*, 724–739. [CrossRef]
32. Wang, Z.Y.; Stern, F. Volume-of-fluid based two-phase flow methods on structured multiblock and overset grids. *Int. J. Numer. Methods Fluids* **2022**, *94*, 557–582. [CrossRef]
33. Rabha, S.S.; Buwa, V.V. Volume-of-fluid (VOF) simulations of rise of single/multiple bubbles in sheared liquids. *Chem. Eng. Sci.* **2010**, *65*, 527–537. [CrossRef]
34. Li, L.M.; Jiang, B.W.; Wei, G.L.; Li, X.J.; Zhu, Z.C. Multiscale multiphase flow simulations using interface capturing and Lagrangian particle tracking. *Phys. Fluids* **2022**, *34*, 121801. [CrossRef]
35. Xu, Y.; Liu, M.; Tang, C. Three-dimensional CFD–VOF–DPM simulations of effects of low-holdup particles on single-nozzle bubbling behavior in gas–liquid–solid systems. *Chem. Eng. J.* **2013**, *222*, 292–306. [CrossRef]
36. Hirt, C.W.; Nichols, B.D. Volume of fluid (VOF) method for the dynamics of free boundaries. *J. Comput. Phys.* **1981**, *39*, 201–225. [CrossRef]

Disclaimer/Publisher's Note: The statements, opinions and data contained in all publications are solely those of the individual author(s) and contributor(s) and not of MDPI and/or the editor(s). MDPI and/or the editor(s) disclaim responsibility for any injury to people or property resulting from any ideas, methods, instructions or products referred to in the content.